Coversheet for EarthArXiv

Origin and fate of methane in the Central American convergent margin

Matteo Selci[1], M. Cascone[1], T. J. Rogers[2], A. Vitale Brovarone[3,4,5], Carlos Ramirez[6], P. Beaudry[7,8], S. Ono[7], M. Yücel[9], G. L. Jessen[10,11], M. O. Schrenk[12], J. M. de Moor[13,14], P. H. Barry[15], A. Cordone[1], K. G. Lloyd[2], and D. Giovannelli*[1,15,16,17,18]

1 Department of Biology, University of Naples Federico II, Naples, Italy
2 University of Tennessee, Knoxville, TN, USA
3 Department of Biological, Geological, and Environmental Sciences, Alma Mater Studiorum Università di Bologna, Bologna, Italy
4 Institut de Minéralogie, de Physique des Matériaux et de Cosmochimie (IMPMC), Sorbonne Université, Muséum National d'Histoire Naturelle, UMR CNRS 7590, IRD UR206, Paris, France
5 Institute of Geosciences and Earth Resources, National Research Council of Italy, Pisa, Italy
6 Servicio Geológico Ambiental (SeGeoAm), Heredia, Costa Rica
7 Department of Earth, Atmospheric and Planetary Sciences, Massachusetts Institute of Technology, Cambridge, MA, USA
8 Department of Earth and Planetary Sciences, Johns Hopkins University, Baltimore, MD, USA
9 Institute of Marine Sciences, Middle East Technical University, Erdemli, Turkey
10 Instituto de Ciencias Marinas y Limnológicas, Universidad Austral de Chile, Valdivia, Chile
11 Centro de Investigación Oceanográfica COPAS COASTAL, Universidad de Concepción, Concepción, Chile
12 Department of Earth and Environmental Sciences, Michigan State University, East Lansing, MI, USA
13 Observatorio Vulcanológico y Sismológico de Costa Rica (OVSICORI), Universidad Nacional, Heredia, Costa Rica
14 Department of Earth and Planetary Sciences, University of New Mexico, Albuquerque, NM, USA
15 Marine Chemistry & Geochemistry Department - Woods Hole Oceanographic Institution, MA, USA
16 Institute for Marine Biological and Biotechnological Resources, National Research Council of Italy (CNR-IRBIM), Ancona, Italy
17 Department of Marine and Coastal Science, Rutgers University, New Brunswick, NJ, USA
18 Earth-Life Science Institute, ELSI, Tokyo Institute of Technology, Tokyo, Japan

***Corresponding author**: Donato Giovannelli, donato.giovannelli@unina.it

Origin and fate of methane in the Central American convergent margin

Matteo Selci[1], M. Cascone[1], T. J. Rogers[2], A. Vitale Brovarone[3,4,5], Carlos Ramirez[6], P. Beaudry[7,8], S. Ono[7], M. Yücel[9], G. L. Jessen[10,11], M. O. Schrenk[12], J. M. de Moor[13,14], P. H. Barry[15], A. Cordone[1], K. G. Lloyd[2], and D. Giovannelli*[1,15,16,17,18]

1 Department of Biology, University of Naples Federico II, Naples, Italy
2 University of Tennessee, Knoxville, TN, USA
3 Department of Biological, Geological, and Environmental Sciences, Alma Mater Studiorum Università di Bologna, Bologna, Italy
4 Institut de Minéralogie, de Physique des Matériaux et de Cosmochimie (IMPMC), Sorbonne Université, Muséum National d'Histoire Naturelle, UMR CNRS 7590, IRD UR206, Paris, France
5 Institute of Geosciences and Earth Resources, National Research Council of Italy, Pisa, Italy
6 Servicio Geológico Ambiental (SeGeoAm), Heredia, Costa Rica
7 Department of Earth, Atmospheric and Planetary Sciences, Massachusetts Institute of Technology, Cambridge, MA, USA
8 Department of Earth and Planetary Sciences, Johns Hopkins University, Baltimore, MD, USA
9 Institute of Marine Sciences, Middle East Technical University, Erdemli, Turkey
10 Instituto de Ciencias Marinas y Limnológicas, Universidad Austral de Chile, Valdivia, Chile
11 Centro de Investigación Oceanográfica COPAS COASTAL, Universidad de Concepción, Concepción, Chile
12 Department of Earth and Environmental Sciences, Michigan State University, East Lansing, MI, USA
13 Observatorio Vulcanológico y Sismológico de Costa Rica (OVSICORI), Universidad Nacional, Heredia, Costa Rica
14 Department of Earth and Planetary Sciences, University of New Mexico, Albuquerque, NM, USA
15 Marine Chemistry & Geochemistry Department - Woods Hole Oceanographic Institution, MA, USA
16 Institute for Marine Biological and Biotechnological Resources, National Research Council of Italy (CNR-IRBIM), Ancona, Italy
17 Department of Marine and Coastal Science, Rutgers University, New Brunswick, NJ, USA
18 Earth-Life Science Institute, ELSI, Tokyo Institute of Technology, Tokyo, Japan

***Corresponding author**: Donato Giovannelli, donato.giovannelli@unina.it

Abstract

Convergent margins are gateways to Earth's interior where volatile species are cycled between the planet's surface and interior. At these locations, carbon is recycled from deep reservoirs in two main forms: oxidized carbon, such as carbon dioxide, and reduced carbon, such as methane. While the former is quantitatively more important and its volcanic fluxes have been better constrained, the latter represents the most reduced form of carbon on Earth and greatly contributes to greenhouse effects and climate stability. Understanding the geological and biological processes underpinning the origin and fate of methane in convergent margins is thus pivotal to constraining carbon cycling and redox balance in convergent margins. Here, we present coupled geochemical and microbiological data from 47 geothermal deeply-sourced seeps spanning the Costa Rica and Panama convergent margin. By analyzing the presence and diversity of methane-cycling microorganisms and using clumped isotope data, we observed that biotic and abiotic processes are both involved in driving the quantity and isotopic signature of methane cycled to the surface, providing an unprecedented snapshot of the geobiological processes controlling methane cycling in convergent margins.

Keywords: Convergent margins, methane cycle, clumped isotopes, deep biosphere, carbon cycle

Introduction

Earth's volatiles are continuously cycled between Earth's surface and deep reservoirs, contributing to maintaining our planet's habitability for at least the last 3.8 billion years[1–4]. Plate tectonics controls volatile recycling mainly through subduction, arc volcanism, and mantle outgassing[5]. Convergent margins, where subduction occurs, are gateways between the oxidized Earth's surface and the reduced

interior[2]. The quantity and speciation of carbon subducted and recycled to the surface affect the redox potential of the Earth's surface and alter the atmospheric composition over geological timescales influencing climate[6,7]. During its ascent from the mantle to the surface, complex geological and biological processes alter carbon's redox state and its mobility and residence time in the mantle, crust, and atmosphere[3,8,9]. At convergent margins, carbon can be released through volcanism and secondary geothermal manifestation in two main forms: oxidized carbon as carbon dioxide (CO_2) and reduced carbon as methane (CH_4)[6]. Other quantitatively less important forms of carbon with intermediate redox oxidation states are also present, such as carbon monoxide (CO) or organic complexes. Carbon dioxide represents the vast majority of the carbon released through volcanism [5], and its origin, global flux, and contribution to Earth's atmospheric composition and climate stability over time have previously been constrained[1,10]. Carbon dioxide released from the subducting slab can be subjected to several processes on its way to the surface: it can be used by subsurface microbial communities, can precipitate as calcite as the result of abiotic or biotic processes and can react with reduced fluids-containing hydrogen-to form graphite and methane, depending on the temperature-pressure and redox conditions[8]. While carbon dioxide at convergent margins has been thoroughly investigated, methane's origin and fate have received comparatively less attention[3,9], and studies have been generally focused on methane released from the seafloor in accretionary margins[11,12]. This is partially due to the much lower concentrations of methane in volcanic gases[13] .

Methane is a powerful greenhouse gas that plays a significant role in regulating Earth's climate. Its global warming potential is 28 times greater than carbon dioxide over a 100-year time frame[14]. Methane is also important for understanding the balance of reducing equivalents in Earth's interior[9], and methane formation, regardless of the processes, consumes electrons removing reducing equivalents from the mantle[6]. Recently, convergent margins have been shown to be the source of large fluxes of deep methane from the mantle to the crust[9]. However, the ultimate fate of the produced methane is unclear, and the biological and abiotic sinks have yet to be identified[15], and methane concentrations in volcanic and hydrothermal gases in arc environments are generally low[13]. For these reasons, a better understanding of the sources and sinks of methane at convergent margins is necessary to improve constraints on carbon cycling and, especially, to assess its role in the development of deep subsurface ecosystems[15,16] . Recently, serpentinization in the forearc region of convergent margins has been shown to produce large fluxes of hydrogen and abiotic methane, which may constitute a significant source of energy to the subsurface biosphere[15]. One of the main goals of this contribution is to assess whether deep sources of methane can be identified.

Methane can be produced through a variety of natural processes, including biotic and abiotic processes such as microbial methanogenesis[17], thermogenic generation in organic matter-rich sedimentary and metasedimentary rocks[18], reduction of carbon species following serpentinization of oceanic mantle rocks—from mid-ocean ridges to subduction—the mantle wedge[15,19] and metamorphism of graphite-bearing rocks[20]. Methane generated deep by subduction processes and shallower in the crust by biological activity might then be transported to the surface by fluids and gases[9]. During ascent, biological and geological processes may alter the quantity and isotopic signature of the released methane, confounding the primary source with secondary processes. Determining the sources and processes of methane formation based solely on carbon ($^{13}C/^{12}C$) and hydrogen (D/H) isotope ratios is challenging since there is substantial overlap in isotopic signatures associated with microbial, thermogenic, and abiogenic gases [20,21].

Recent advances in doubly substituted (clumped) methane isotopologue analyses provide a key tool to estimate the temperature at which methane was formed or thermally equilibrated, unlocking critical information on the origin of methane in geological reservoirs[22]. The abundance and isotopic

composition of methane have been reported for hot springs and volcanic-hosted geothermal systems in recent years[23–28], revealing significant variability in the isotopic signature of methane in volcanic-hosted systems. Multiple hypotheses have been proposed to explain the results, including abiotic generation from mantle-derived CO_2, pyrolysis of organic matter in high-temperature geothermal systems, thermogenic origin from surface-derived or ancient organic matter, microbial production from mantle-derived CO_2 or surface-derived sources of carbon, or a combination of the above[23–28]. The large variability in isotopic signatures observed in geothermal systems has not been systematically linked to any measured variable, and a clear picture of the origin of methane and secondary geological and biological processes altering its quantity and isotopic composition at convergent margins is still lacking.

Here, we report results on the gas geochemistry, methane isotopologues, aqueous geochemistry, and microbiology from 47 deeply-sourced seeps (*sensu*[29] spanning the Costa Rica and Panama convergent margins). We link the subsurface and near-surface microbial community involved in methane cycling to gas, aqueous, and solid phase geochemistry, lithology and to methane isotopologues data across diverse rock reservoirs of the Central American convergent margin (Figure 1 and Supplementary Table S1). In this area, the Cocos and the Nazca plates subduct beneath the Caribbean plate, controlling latitudinal gradients in the degree of distension and compression in the upper plate, diversification of volcanic activities, the distribution of sedimentary basins, and the development of a backarc thrust belt[30]. Our results show that the shift in methane isotopologue compositions is consistent with overlapping geological and biological processes controlled by the geological settings and dominant rock type present at each sample location, ultimately showing that complex feedback between deep and surface Earth processes control the origin and fate of methane in the Central American convergent margin.

Materials and Methods

Sampling approach

We collected 47 gas and water samples from diverse geothermal features, collectively called deeply-sourced seeps[29], across a 700 km section of the Central American convergent margin[8,31–33]. These features included geothermal springs, steam heated waters, mud pools, fumaroles, acid-sulfate springs, sodium chloride springs, bicarbonate springs, and alkaline springs. We used field observation, pH, and temperature measurements to identify the main inlet in each seep and collected samples close to minimize surface contamination[29]. Gas phase samples and water samples were collected in pre-evacuated 250 mL Giggenbach bottles containing 50 mL of 4 M NaOH. Gas samples for methane clumped isotopologue determination were either collected into 1L pre-evacuated glass bottles containing ~ 200 mL 4 M NaOH (high-temperature, high flux samples with low methane concentration) or in 250 ml serum vials filled with distilled water, which was then entirely replaced by injecting gas (low-temperature bubbling springs with high methane concentration). Gas for noble gas analysis was collected in copper tubes as previously described[34]. Suspended cells in hydrothermal fluids (up to 2 L) were collected using a 0.22 µm sterivex® filter, while ca. 30 g of sediments were collected into a sterile centrifuge tube. All samples were quick-freeze in liquid nitrogen for transport and downstream analysis. Major ion measurements were performed on filtered (0.22 µm) subsamples and stored at 4 °C. Samples for carbon isotope analysis of dissolved inorganic carbon (DIC) were collected in acid washed 15 mL borosilicate vials, crimp-sealed with butyl rubber stoppers, and stored in dark at 4 °C until laboratory analysis.

Gas geochemistry

Giggenbach bottle samples for gas composition were analyzed as previously described [35]. Briefly, the bottles were connected to a Gas Chromatograph (GC) model Agilent 7890A via a vacuum line and turbo pump. The headspace gas was transferred to the GC through two parallel columns using two 250 µL loops and two 6-way valves switching simultaneously. One column operated with Ar carrier gas and the other with H_2 carrier gas. Methane was measured on the H_2 carrier gas column with a flame ionization detector, and other gasses were analyzed on a thermal conductivity detector. The methane concentration in water samples was calculated from the mass of water collected and the partial pressure of methane measured in the headspace. The CO_2/CH_4 ratio in gas samples was determined by calculating the total moles of CO_2 and CH_4 collected in the Giggenbach bottle. The error for CH_4 concentrations and CO_2/CH_4 ratios was estimated at less than 5 % and less than 10 %, respectively.

Methane clumped isotopes

Methane isotopologues (i.e. $^{12}CH_4$, $^{13}CH_4$, $^{12}CH_3D$, and $^{13}CH_3D$) were analyzed as previously described[36]. Briefly, methane was extracted and purified from the gas phase of the pre-evacuated glass bottles by repeatedly vacuuming and flushing with a He carrier gas through a cold trap (submerged in liquid nitrogen) filled with activated charcoal, trapping CH_4, N_2, CO, and traces of CO_2. The trap was then heated to separate adsorbed gasses into the gas chromatograph using a Carboxen-1000 packed column (MilliporeSigma, St Louis, MI) held at 30 °C, and the eluted methane was trapped again in a U-trap containing silica gel at liquid nitrogen temperature. The purified CH_4 samples were measured for $^{12}CH_4$, $^{13}CH_4$, $^{12}CH_3D$, and $^{13}CH_3D$ isotopologue composition using a tunable infrared laser direct absorption spectroscopy (TILDAS) instrument [36,37]. Samples were bracketed by measurements of methane standard gasses of known isotopic composition (δD and $\delta^{13}C$) spanning a large δD range (~200 ‰), which were heated to 250 °C for at least two weeks with a Pt catalyst to ensure isotopologue equilibrium. Isotope values are reported using standard delta notation against VPDB and VSMOW for the ratios $^{13}C/^{12}C$ and D/H, respectively. This isotope scale was calibrated by the measurements of NGS-1 and NGS-3, using reference $\delta^{13}C$ values of −29.0 and −72.8 ‰, and δD of −138 and −176 ‰, for NGS-1 and NGS-3, respectively.

Noble Gas Geochemistry

Copper tube samples were connected to the extraction line using an O-ring connection and ~5 cm3 of gas was expanded into the cleanup line. The pressure was measured using a capacitance manometer and then a small aliquot of gas was expanded into the cleanup portion of the line. Reactive gases were chemically removed by exposing gases to a titanium sponge held at 650 °C. The titanium sponge was then cooled for 10 min to room temperature in order to getter hydrogen before gases were expanded to a dual hot (SAES ST707) and cold (SAES ST707) getter system, held at 250°C and room temperature, respectively. Another small aliquot of gas was then segregated for preliminary analysis on a quadrupole mass spectrometer (QMS). Noble gases were separated using a series of cryogenic traps, cooled using helium compressors. The heavy noble gases (Ar–Kr–Xe) were adsorbed at 30 K onto a nude stainless steel trap and He and Ne were adsorbed at 10 K on a charcoal trap. The temperature of the charcoal trap was then raised to 30 K, releasing only He, which was then inlet into the Noblesse mass spectrometer. Following He abundance and isotope determination, the temperature on the charcoal cryogenic trap was raised to 80 K for 15 min to release Ne, which was inlet into the Noblesse mass spectrometer. Following Ne isotope measurement, the nude and charcoal cryogenic traps were raised to 300 K for cleanup. Air-standards were analyzed daily from an air cylinder collected on the roof of the Clark Laboratory building on WHOI's Quissett campus on 15 September

2020. Air-standards are fully automated and run overnight, following sample analysis during the day. Air-standards were run for He and Ne using an identical method to the one employed for samples. Air-standards were measured over a concentration range which spanned two orders of magnitude, to account for any non-linearity of the system. Full procedural blanks were run weekly; average (mean) ^{4}He blanks and ^{20}Ne blanks were less than 5 % of the sample size. Doubly-charged ^{40}Ar++ was monitored but because it can be resolved from 20Ne, no correction was applied. Likewise, no CO_2++ correction was applied to ^{22}Ne, because CO_2 backgrounds were at the detection limit and thus corrections were considered insignificant. Water samples were processed on the same extraction line as gas samples; however the inlet procedure was slightly different. Cu tube samples were interfaced to the extraction system in an identical fashion. Approximately 13 ml of water was inlet and then degassed under vacuum using a magnetic stirrer in a glass bulb beneath the Cu tube inlet area. Noble gases were then quantitatively transferred into a smaller volume using the capillary method. Water vapor in the extraction line was cryogenically drawn across a capillary towards a stainless-steel cold trap cooled to liquid nitrogen temperature (−196 °C). The consistent flow of water vapor towards the colder water trap effectively entrains the noble gases and quantitatively draws them into the cold trap, along with a small portion of the water vapor. The consistency of this flow prevents any backflow of noble gases, such that they are quantitatively transferred into this cold trap volume[38]. He and Ne were then inlet into the purification portion of the line (i.e., with Ti and SAES getters) for cleanup and noble gas separation in an analogous fashion to what is described above for gas samples. Helium isotope results (^{3}He/^{4}He of sample = R_C) from this study are reported relative to air (R_A), corrected for the occurrence of atmospheric He (to R_C/R_A) and blank contributions, which are consistently less than 5 %.

Aqueous and sediment geochemistry

Dissolved anions and cations were determined via ion chromatography. A Dionex AS4A-SC separation column, sodium hydroxide eluent, and ASRS-I suppressor were used for anions. In contrast, a Dionex CS12-SC separation column, methane sulfonic acid eluent, and CSRS-I suppressor were used for cations.

Genomic DNA extraction and sequencing

DNA extractions were performed from filters using a modified phenol-chloroform extraction optimized for low biomass samples based on previously published methods[39], with additional modifications for use with Sterivex filters[33]. Briefly, extractions were performed via chemical lysis with lysozyme, proteinase-K, and SDS treatment, then purified with phenol-chloroform extractions and precipitated with sodium acetate and isopropyl alcohol. DNA extractions from sediment samples were performed using the Qiagen DNeasy PowerSoil HTP 96 Kit. Difficult/low-yield samples were extracted using a modified phenol-chloroform extraction followed by concentration using the Zymo Genomic DNA Clean and Concentrator Kit (Zymo). Extracted DNA was quantified using a NanoDrop 2000c with additional polymerase chain reaction screening using universal bacterial primers. High-quality DNA was extracted from the fluids and sediments of the majority of the 47 sites; 31 sites worked for both fluids and sediments, 5 were successful only in sediments, and 10 only in fluids. Amplicon sequencing and shotgun metagenome sequencing were performed as part of the Census of Deep Life initiative with the Deep Carbon Observatory on an Illumina MiSeq platform at the Marine Biological Laboratory sequencing facility (https://www.mbl.edu/). Amplicon sequencing was carried out after amplifying the bacteria-specific V4-V5 region of the 16S rRNA gene using primers 518F (AATTGGANTCAACGCCGG) and 926R (CCGYCAATTYMTTTRAGTTT). The same extracted DNA was used for shotgun metagenomic sequencing without amplification using the

Illumina Nextera Flex kit for MiSeq+NextSeq. Shotgun metagenomes varied from 25 to 150 million base pairs. The amplicon sequencing data is available from the NCBI SRA archive under accession number PRJNA579365, while the shotgun metagenomes are deposited under project number PRJNA627197.

Bioinformatic and statistical approaches

Raw reads received from the sequencing center were processed using the DADA2 package [40]. Primers and adapters were trimmed, followed by a quality profile step, where only sequences with a call quality for each base between 20 and 40 were kept for further analysis. Amplicon sequence variants (ASVs) were estimated through error profile, and taxonomy was assigned to the SILVA database release 138.1[41]. The resulting taxonomic assignments, in combination with variant abundance tables, were used with the Phyloseq package[42]. Sequences related to Chloroplasts, Mitochondria, and Eukaryotes, as well as groups related to human pathogens and common DNA extraction contaminants[43], were removed from the dataset. All downstream statistical analyses, data processing and plotting were carried out in the R statistical software version 4.2.2. Shotgun Metagenomic short reads were quality checked and trimmed using Trimmomatic[44], and then functionally annotated with Mifaser[45] using the provided Gold Standard Plus (GS21 ALL) database, including gene sequences from biogeochemically relevant pathways. Post QC raw reads were used to assess the taxonomic composition with a sensitive profiling tool called Kaiju[46]. The obtained count tables were imported in R. To account for the influence of different gene lengths on the read recruitments, and for the different sequencing depth associated with each metagenome, read counts were normalized to the average length of the corresponding protein in the GS21-ALL database and multiplied by the median library size across the dataset. To account for the compositionality of sequencing data, we further divided each EC abundance by the abundance of the DNA directed RNA polymerase subunit β (rpoB gene), and scaled to 1,000,000. This procedure returns the relative abundance of each EC for 1,000,000 reads mapped to rpoB, assuming equal sequencing depth. This allows within-sample and between-sample comparison, effectively opening the data and removing the problem of compositionality. The obtained normalized counts (mifaser_nrpo) were used for downstream analyses.

A complete R script containing all the steps to reproduce our analysis is available at https://github.com/giovannellilab/Selci_et_al_Origin_and_fate_of_methane and is released as a permanent version using Zenodo with doi: 10.5281/zenodo.14617229.

Results

To understand the origin, the fate, and the distribution of methane seeps, 16S rRNA gene amplicon libraries for methane-cycling microbes and metagenomic DNA sequences of key genes for methane cycling were compared to the methane isotopic signatures observed in 47 seeps sampled along the Central America convergent margin (Figure 1A). Methane was detected in 36 sites, in concentrations high enough to obtain clumped isotopologue measurements in 11 sites (Supplementary Table S2). The deeply sourced seeps that were sampled cover the major volcanic provinces across the Central American convergent margin: the outer forearc, the forearc, the volcanic arc and the backarc. Seeps positioned at each location show differences in the origin of the volatiles as revealed by helium isotope systematics, with near arc sites showing higher Rc/Ra ratio compared to forearc and backarc (Supplementary Figure S1). The sampled seeps are also located in geologic units characterized by different lithological assemblages, including ocean floor basalts, quaternary sedimentary deposits, sedimentary rocks, and volcanic rocks (Figure 1B). The distribution of the different lithologies is partially related to the location with respect to the across-subduction axis, with ocean seafloor basalt

present in the outer forearc, volcanic rocks in the main volcanic arc and deep in the forearc province, sedimentary rocks associated with uplifting and orogenic events, and quaternary sedimentary deposits filling the basins at the margin of the forearc and backarc created by the local topography (Figure 1B).

Methane concentrations range from 9×10^{-5} to 864 mmol/mol of total dry gas (Table 1). Values for $\delta^{13}C_{CH4}$ range from -22.5 to -76.3 ‰. Methane cycling microorganisms, recognized based on their taxonomic annotation, were identified in nearly all sites that yielded amplifiable DNA (43 out of 47 sites) with the exception of BQ, HN, and SR. Sequences associated with known methane cycling microorganisms constitute in total 5.2 % of all identified ASVs, ranging between 0.01 % (RRS) and 36.2 % (LWF) of the total sequences, identified in 69 samples, of which 34 were fluids. The community was highly diverse, and represented by members of the major Bacteria and Archaea orders known to be involved in methane cycling, either through methanogenesis or methane oxidation (both aerobic and anaerobic).

To better understand methane formation mechanisms, we measured the relative abundance of the doubly substituted (i.e. "clumped") isotopologue $^{13}CH_3D$ (Figure 2A). All sites, with the exception of CI and BR1, plot near known formation mechanisms, in broad agreement with their placement in a Whiticar plot (Supplementary Figure S3). Samples like PS, LW, and CW fall within the "bacterial carbonate reduction" field (hydrogenotrophic methanogenesis) resulting in an isotopically low $\delta^{13}C$ signal, as found in pore waters and gas hydrates of marine sediments[36]. SI and SR are placed within the "bacterial methyl type and fermentation" field (methylotrophic and acetoclastic methanogenesis) which is D-depleted compared to the other (Supplementary Figure S3). Samples BQ, HN, QN, BR1, and CI are enriched in ^{13}C and D, falling within the geothermal and thermogenic fields. Sample MT falls within the "mix and transition" field, with intermediate δD_{CH4} and $\delta^{13}C_{CH4}$, suggesting mixing of different methane sources.

Among the samples related to hydrogenotrophic methanogenesis (HM; Figure 2A), only PS ($\Delta^{13}CH_3D$=5.65 ‰) yields a $\Delta^{13}CH_3D$ similar to the microbial methane measured in pore waters and gas hydrates from the northern Cascadia margin[36], which is also in line with the expected low formation temperatures in marine sediment basins. In PS sediments, anaerobic methane microbes have the highest abundance (Supplementary Figure S4C, S4D) with Methanosarcinales and ANME-1 forming the dominant groups. LW and CW samples are lightly depleted in $^{13}CH_3D$ ($\Delta^{13}CH_3D$=4.68 ‰ and $\Delta^{13}CH_3D$=4.48 ‰) showing $\Delta^{13}CH_3D$-based temperatures not congruent with their expected formation temperatures. In the LW fluids, aerobic methane oxidizers are dominant against the anaerobic groups, highlighted by the higher abundance of Rhizobiales compared to the Methanosarcinales (Figure 2B, C). In LW sediments, instead, anaerobic methane microbes are the dominant groups (Supplementary Figure S4C, D) with Methanosarcinales and Methanomassiliicoccales as the most abundant taxa (Supplementary Figure S2). As LW, also CW sediments are characterized by known anaerobic methane cyclers (Figure 2B, C) such as Methanosarcinales, Methanomassiliicoccales, and Methanobacteriales (Supplementary Figure S3C, D). Likewise, CW fluids are dominated by anaerobic methane cyclers such as Methanosarcinales and Methanobacteriales, with the addition of the aerobic group of the Rhizobiales.

Samples related to methylotrophic and acetoclastic methanogenesis (SI, and SR) as well as the "mix and transition" field (MT; Supplementary Figure S3) are highly depleted in $^{13}CH_3D$ ($\Delta^{13}CH_3D$=-0.59 ‰, $\Delta^{13}CH_3D$=0.28 ‰, and $\Delta^{13}CH_3D$=1.58 ‰, respectively) similarly to swamp and cow rumen samples[36]. These low $\Delta^{13}CH_3D$ values correspond to unrealistically high $\Delta^{13}CH_3D$ temperatures which indicate the absence of a thermodynamic equilibrium[36,47]. In SI, kinetic isotopic effects may be caused

by the major presence of anaerobic methane oxidizers (Supplementary Figure S4D), which are dominated by Methanosarcinales, Methanobacteriales, and Methanomassiliicoccales. In a similar way, in MT, anaerobic methane oxidizers are dominant compared to the aerobic ones (Figure 2B,C) with Methanosarcinales as the main taxa detected.

Samples associated with thermogenic methanogenesis *i.e.,* BQ, QN, and HN, yielded consistently low $\Delta^{13}CH_3D$ values ($\Delta^{13}CH_3D$=1.65 ‰, $\Delta^{13}CH_3D$=1.76 ‰, and $\Delta^{13}CH_3D$=1.46 ‰, respectively). These values are in the range of similar geothermal systems[48] which correspond to high $\Delta^{13}CH_3D$-based temperatures. Among them, only in QN microbes related to methane transformations are detected, with a major abundance of anaerobic groups (Figure 2C). These are mainly composed of ANME-1 and Methanosarcinales in the fluids while aerobic methane microbes dominate in the sediments represented by Methylococcales and Betaproteobacteriales (Supplementary Figure S4C). Although BR1 fell within the thermogenic $\delta^{13}C_{CH4}$ zone in the Whiticar plot (with a value of -26.7 ‰) similar to BQ, HN and QN (-29.9 ‰, -22.5 ‰, and -28.5 ‰), it showed an enrichment in $^{13}CH_3D$ (3.48 ‰), suggesting isotopic equilibrium of CH_4 with dissolved CO_2 via anaerobic methane oxidation under submolar sulfate concentrations[49,50]. In BR1, a concentration of 0.44 mM of sulfate is detected consistent with the previous hypothesis since anaerobic methane oxidation can use sulfate as an electron acceptor, however a higher abundance of aerobic methane microbes is found (Figure 2B, C) with Methylomirabiales and Methylococcales as dominant groups in both fluid and sediment samples (Supplementary Figure S4). CI shows light $\delta^{13}C_{CH4}$ fingerprint (-41.6 ‰) but the highest $\Delta^{13}CH_3D$ (8.32 ‰), suggesting kinetic isotopologue fractionation (non-equilibrium clumped value) as a potential reason. This may be related to the prevalence of anaerobic methane microbial groups (Figure 2C) in fluid samples which are dominated by Methanosarcinales unlike the sediment sample where Methanobacteriales is the highest in abundance (Supplementary Figure S2).

Looking at key genes (i.e., methanogenesis and methane oxidation) associated with the methane cycle, we considered sequences encoding methyl-coenzyme M reductase (*mcrA*), the enzyme responsible for the last step of the biological methane formation by the reduction of a methyl group[51,52] and the formylmethanofuran dehydrogenase (*fwd*), a key enzyme at beginning of the pathway for the CH_4 formation from H_2/CO_2 [53] (Supplementary Figure S5). For aerobic methane oxidation, the two evolutionarily related enzymes methane monooxygenase (*mmo*) and the methane/ammonia monooxygenase (*pmo-amo*)[54] are included. The methanol dehydrogenase (*mdh*) is also considered since it is a key intermediate in methylotrophic metabolism in which one-carbon (C1) compounds are reduced[55]. While these genes were identified in the majority of the investigated metagenomes (n= 43 sites), their abundance is higher in sites with high methane concentrations measured in the gas phase. In PS sediments, the methanogenesis genes *mcrA* and *fwd* displayed the highest abundance compared to those (*i.e.*, *mmo*, *pmo-amo*, and *mdh*) involved in the methane oxidation and post methane oxidation pathways, suggesting an overproduction of biological methane against its utilization. Gene sequences related to the methane utilization like the *mmo* and the *pmo-amo* are found in highest abundance in both LW and CW fluids, as well as for the gene of the *mdh*. The highest abundance of sequences that encode *mcrA* is found, instead, within the LW and CW sediments, followed by the sequences for *fwd*.

MT fluids are characterized by a higher number of methanogenesis related gene sequences compared to those involved in methane oxidation. In SI, high content of sequences related to *mcrA* and *fwd* were found in sediments while fluids communities showed mainly potential for methanol oxidation (*mdh*). In BQ, sequences associated with *fwd* and *mdh* dominate in both fluid and sediments, but the fluids also contain *mcrA* sequences and smaller amounts of *pmo-amo* and *mmo*. In a similar way, QN

displayed a high number of sequences in fluids and sediments related to methane oxidation (high abundance in *mmo*, *pmo-amo*, and *mdh*) rather than methane formation processes. In BR1, fluids and sediments are both characterized by high quantities of *mmo* and *pmo-amo* sequences, while rather few *mcrA* sequences were found only in fluids. Similarly, CI fluids are dominated by sequences for methane oxidation (*mmo* and *pmo-amo*). CI sediments displayed instead a main presence of sequences related to CO_2 utilization and methanol oxidation (*fwd* and *mdh*). Finally, comparing the distribution of the key methane cycling functional genes on the clumped isotope $\Delta^{13}CH_3D$ in relation to $\delta^{13}C_{CH4}$ (Figure 3; Supplementary Figure S6) is consistent with the distribution of the taxonomic assignment presented in Figure 2C and 2D.

When looking at the distribution of functional genes annotated at each site using jaccard based PCoA multivariate ordinations (Supplementary Figure S7), a clear partition between fluids and sediments emerges (adonis p.value<0.0001; Supplementary Figure S7C and S7D), both in the unweighted and weighted ordination. This is consistent with the dual distribution between the subsurface and surface community metabolic profiles along the Central America convergent margins. The different bedrock associated with each sampling site are also statistically significant (adonis, p<0.001; Supplementary Figure S7A and S7B) and the percentage of variance explained was 16.2 % and 38.1 % for the weighted and unweighted Jaccard based PCoA, respectively. When considering only the enzymes involved in methane cycling, the percentage of explained variance increases to 29.3 % and 71.2 % for the weighted and unweighted Jaccard based PCoA, respectively. The difference between fluid and sediment persists when considering methane cycling genes (adonis p-value<0.005), suggesting a distinct role of methane cycling in both the matrices, although the different bedrock composition was also significative (Figure 4A; adonis, p.value<0.0001), for both the weighted and unweighted ordination (Supplementary Figure S8A and S8B). The deeply sourced seeps distributed in quaternary deposits (QD) showed a similar functional composition, consistent with similar lighter $\delta^{13}C_{CH4}$ and a strong biogenic methane signal (Figure 4B). A different trend is observed with the seeps distributed along the central regions of Costa Rica and Panama, characterized by sedimentary and volcanic rocks (SR and VR) where the methane emissions had a thermogenic/abiotic signature (Figure 4B, Figure 2A).

The potential origin of the methane and CO_2 was also depicted by the relative isotopic compositions of He compared to CO_2 and CH_4. In the ternary diagram of CO_2, ^3He and ^4He (Figure 4C) most of the samples located within the volcanic rock reservoirs are characterized by higher mantle contributions ($^3He/^4He$ ratio above air) and only in two samples (BC and PF), located in Panama and in the Costa Rica backarc respectively, an enrichment in crustal CO_2 above average arc samples is observed (Figure 4C). Samples from sites hosted in sedimentary rocks and quaternary deposits are instead enriched in radiogenic helium on average compared to volcanic rock hosted samples. He isotopes and CH_4 ternary (Figure 4D) show an increase in CH_4 concentrations in volcanic rock hosted samples from a mantle-like source, while a clear enrichment in CH_4 in some of the sites hosted in quaternary deposits.

Discussion

Convergent margins are key locations for the recycling of volatiles between the Earth's surface and interior[2]. Because carbon dioxide represents the vast majority of the carbon released through volcanism[5], its origin, global flux and contribution to Earth's atmospheric composition and climate stability through time has been relatively well constrained with global fluxes from subaerial volcanoes

equal to ~300 Mt yr^{-1} of CO_2[56]. By contrast, methane's origin and fate at convergent margins has received comparatively less attention[9], and studies have been generally focused on methane released underwater in accretionary prisms[11,12]. Additionally, although the carbon budget of volcanic arcs has been investigated in detail in the last two decades, information regarding the origin and fate of carbon recycled in the outer forearc, forearc, and backarc regions are scarce[8]. Understanding the relative contribution of methane recycled at convergent margins as well as their relative origins is a key step in constraining global carbon cycling.

While several studies have investigated the origin of methane in diverse tectonic settings[25,28], detailed information on the origin of methane at convergent margin is limited to a few data points [23–28] that reveal a high variability in the isotopic signature of methane in volcanic hosted systems. Additionally, the biological overprint imposed by the large subsurface biosphere present in the crust[57] has been neglected so far. Biology has been shown to play a key role in altering the characteristics and quantity of CO_2 recycled in the forearc[32,33] and backarc regions[58] of convergent margins, suggesting a potential role in methane cycling as well. Our new gas geochemistry and clumped methane isotopologue data coupled to metagenomic-based microbial diversity data from subaerial deeply-sourced seeps of the Central America convergent margin provide important constraints on the linkages between biology and subduction.

Our results show that methane is present and detectable in the majority of the sampled seeps distributed across the 700 km segment of the Central America convergent margin (Table 1). While the concentrations of methane vary by 6 orders of magnitude in the sampled seeps, the highest concentrations of methane are at sites hosted in sedimentary quaternary deposits (Figure 1B and Figure 4). Microbial diversity and functional data suggest that the communities present in the sites hosted in quaternary deposits have the potential to be significant contributors to the observed methane (Figure 3, 4 and Supplementary Figure S2), similar to sites hosted in ocean floor basalts. This observation is consistent with the predicted biological origin of the methane using clumped isotope data (Figure 2), similar to methane produced by hydrogenotrophic or methylotrophic and acetoclastic methanogens. Conversely, sites present in volcanic and sedimentary rocks show a higher potential for aerobic and anaerobic oxidation of methane (Figure 3, 4 and Supplementary Figure S2), especially considering that the higher abundance of sequences related to known methane cycling microorganisms is present in these sites in surface sediments, rather than in the deep-derived fluids (Supplementary Figure S2). Taken together our observations suggest that the sampled sites belong to four distinct categories with regard to the methane origin, broadly coinciding with the bedrock type each seep is hosted in (Figure 4).

The first group is composed of ocean floor basalt and other mafic rocks where the presence of highly reduced fluids with high pH suggests the potential for the upflow of serpentinization fluids supporting biological methanogenesis, mainly linked to hydrogen oxidation and the use of deeply derived CO_2. This observation is broadly in agreement with methane and microbiological data reported from other mafic and ultramafic ecosystems (17, 51). The second group is represented by sites hosted in quaternary sedimentary deposits where the redox conditions and concentration of organic carbon likely support methylotrophic and acetoclastic methanogenesis, as supported by our clumped isotope and metagenomic results. In this group the source of carbon for methanogenesis is likely surface-derived and linked with paleo-deposition, although He isotope values suggest the presence of volatiles of deeper origins (Supplementary Figure S1), potentially suggesting that in the case of hydrogenotrophic methanogenesis, which appears to be minor in these sites, deeply-derived CO_2 could directly contribute to the starting carbon pool[8]. The third group is composed of sites hosted in

sedimentary rocks (Figure 1 and Figure 4). The microbial community identified in the fluids of these sites is composed of sequences related to diverse methanogens and less frequently anaerobic methanotrophs (like sequences related to the order Methylomirabilales), suggesting that methane in these sites might be biological in nature, potentially derived from a mix of carbon released from the sedimentary rocks as well as the conversion of deeply-derived CO_2. The clumped isotopes, available for a single site in this category, CI, suggest that this site might be influenced by anaerobic methane oxidation[61], while the Whiticar plot suggests a thermogenic origin for the methane (Supplementary Figure S3). In these sites our data suggests the potential for biological cryptic methane cycling, with unknown effects on clumped isotopes signature. The last group of sites is represented by seeps hosted in volcanic rocks (Figure 1 and Figure 4). These sites show a stronger signal of deeply-derived carbon and helium with varying degrees of mantle influence (Figure 4C and Supplementary Figure S1), suggesting a potential deep origin of the methane[9] or methane derived abiotically or thermogenically from deep CO_2. The clumped isotopes of methane in these sites suggest a thermogenic/abiotic origin, with possible deviation from the expected CH_4 isotopic values likely due to methane utilization near or at the surface (Figure 2 and Figure 3). In these sites biology is represented mainly by sequences related to known methane oxidizers, an observation supported also by the abundance of key genes involved in methane oxidation in the metagenomic data, suggesting the potential of overprinting of the geological signal. A significant role of biology in controlling the origin and fate of the methane is indicated by the $\delta^{13}C$ and δD values of methane of the first two groups, and linked to a biological production that might overprint any deep abiotic signal.

Overall our data show a strong overprint of near surface biological processes on the origin of methane at convergent margin predicted using clumped isotopes and the microbiological data collected at the same sites. Moreover, our results suggest that the host rock type as well as the position within a specific province in the convergent margin (*i.e.*, outer forearc, forearc, arc, and backarc) exerts a strong control over the quantity and signature of the methane cycled to the surface. Previous studies on the origin and fate of CO_2 in this segment of the Central American convergent margin showed that, together with the (possibly biologically) mediated precipitation of calcite, the nature of the subducting plate was one of the major controls on the measured carbon at the surface[8,32,33]. Our results instead suggest that the overriding plate might bear a larger influence on the origin of the methane reaching the surface.

Taken together the data presented show that the geological setting is one of the main factors in controlling the last steps of the carbon path through the Earth's crust before the release within the atmosphere, and that geological and biologically mediated secondary processes can in part overprint the deeper signal and influence the fate of methane at convergent margins. Future studies are needed in order to assess the quantitative contribution of the different processes to the convergent margins methane flux. We expect that the diversity of rock types and geological settings in the overriding plate might exert a similar control on the origin and fate of methane across all subduction zones, with potentially large implications for global methane cycling as well as atmospheric contribution through deep time.

Acknowledgments

Field campaigns and sample collection were possible through support from the Alfred P. Sloan Foundation and the Deep Carbon Observatory (G-2016-7206) to P.H.B., J.M.d.M, D.G. and K.G.L., with DNA sequencing from the Census of Deep Life. This work was supported by funding from the

European Research Council (ERC) under the European Union's Horizon 2020 research and innovation program Grant Agreement No. 948972—COEVOLVE—ERC-2020-STG to DG. Additional support came from The National Fund for Scientific and Technological Development of Chile (FONDECYT) Grant 11191138 (The National Research and Development Agency of Chile, ANID Chile), COPAS COASTAL ANID FB210021 to GJ. DG and AVB were also supported by PRIN project Hydecarb (PRIN 20224YR3AZ). P.H.B., J.M.d.M, and K.G.L. were supported by NSF grant 21211637.

Data Availability Statement

The amplicon sequencing data is available from the NCBI SRA archive under accession number PRJNA579365, while the shotgun metagenomes are deposited under project number PRJNA627197. The code and data to reproduce the analysis is available on GitHub and released through Zenodo https://doi.org/10.5281/zenodo.14617229.

Competing Interest Statement

The authors declare no competing interests.

Classification

Earth, Atmospheric, and Planetary Sciences

References

1. Pearson, P. N. & Palmer, M. R. Atmospheric carbon dioxide concentrations over the past 60 million years. *Nature* **406**, 695–699 (2000).
2. Kelemen, P. B. & Manning, C. E. Reevaluating carbon fluxes in subduction zones, what goes down, mostly comes up. *Proc. Natl. Acad. Sci. U. S. A.* **112**, E3997-4006 (2015).
3. Bekaert, D. V. *et al.* Subduction-Driven Volatile Recycling: A Global Mass Balance. *Annu. Rev. Earth Planet. Sci.* **49**, null (2021).
4. Moore, E. K., Jelen, B. I., Giovannelli, D., Raanan, H. & Falkowski, P. G. Metal availability and the expanding network of microbial metabolisms in the Archaean eon. *Nat. Geosci.* **10**, 629–636 (2017).
5. Aiuppa, A., Fischer, T. P., Plank, T. & Bani, P. CO2 flux emissions from the Earth's most actively degassing volcanoes, 2005–2015. *Sci. Rep.* **9**, 5442 (2019).
6. Hayes, J. M. & Waldbauer, J. R. The carbon cycle and associated redox processes through time. *Philos. Trans. R. Soc. B Biol. Sci.* **361**, 931–950 (2006).

7. Plank, T. & Manning, C. E. Subducting carbon. *Nature* **574**, 343–352 (2019).
8. Barry, P. H. *et al.* Forearc carbon sink reduces long-term volatile recycling into the mantle. *Nature* **568**, 487 (2019).
9. Vitale Brovarone, A. *et al.* Subduction hides high-pressure sources of energy that may feed the deep subsurface biosphere. *Nat. Commun.* **11**, 3880 (2020).
10. Owen, R. M. & Rea, D. K. Sea-Floor Hydrothermal Activity Links Climate to Tectonics: The Eocene Carbon Dioxide Greenhouse. *Science* **227**, 166–169 (1985).
11. Judd, A. G. The global importance and context of methane escape from the seabed. *Geo-Mar. Lett.* **23**, 147–154 (2003).
12. Jahren, A. H., Conrad, C. P., Arens, N. C., Mora, G. & Lithgow-Bertelloni, C. A plate tectonic mechanism for methane hydrate release along subduction zones. *Earth Planet. Sci. Lett.* **236**, 691–704 (2005).
13. Giggenbach, W. F. Redox processes governing the chemistry of fumarolic gas discharges from White Island, New Zealand. *Appl. Geochem.* **2**, 143–161 (1987).
14. Change, I. C. The physical science basis. *Contrib. Work. Group Fifth Assess. Rep. Intergov. Panel Clim. Change* **1535**, 2013 (2013).
15. Vitale Brovarone, A. *et al.* Subduction hides high-pressure sources of energy that may feed the deep subsurface biosphere. *Nat. Commun.* **11**, 3880 (2020).
16. Fullerton, K. M. *et al.* Effect of tectonic processes on biosphere–geosphere feedbacks across a convergent margin. *Nat. Geosci.* **14**, 301–306 (2021).
17. Lever, M. A. A New Era of Methanogenesis Research. *Trends Microbiol.* **24**, 84–86 (2016).
18. Stolper, D. A. *et al.* Formation temperatures of thermogenic and biogenic methane. *Science* **344**, 1500–1503 (2014).
19. Schrenk, M. O., Brazelton, W. J. & Lang, S. Q. Serpentinization, Carbon, and Deep Life. *Rev. Mineral. Geochem.* **75**, 575–606 (2013).
20. Etiope, G. & Sherwood Lollar, B. Abiotic Methane on Earth. *Rev. Geophys.* **51**, 276–299 (2013).
21. Fiebig, J. *et al.* Calibration of the dual clumped isotope thermometer for carbonates. *Geochim. Cosmochim. Acta* **312**, 235–256 (2021).

22. Douglas, P. M. J. *et al.* Methane clumped isotopes: Progress and potential for a new isotopic tracer. *Org. Geochem.* **113**, 262–282 (2017).
23. Moran, J. J. *et al.* Dual stable isotopes of CH4 from Yellowstone hot-springs suggest hydrothermal processes involving magmatic CO2. *J. Volcanol. Geotherm. Res.* **341**, 187–192 (2017).
24. Wang, D. T., Reeves, E. P., McDermott, J. M., Seewald, J. S. & Ono, S. Clumped isotopologue constraints on the origin of methane at seafloor hot springs. *Geochim. Cosmochim. Acta* **223**, 141–158 (2018).
25. Stolper, D. A. *et al.* The utility of methane clumped isotopes to constrain the origins of methane in natural gas accumulations. *Geol. Soc. Lond. Spec. Publ.* **468**, 23–52 (2018).
26. Suda, K. *et al.* The origin of methane in serpentinite-hosted hyperalkaline hot spring at Hakuba Happo, Japan: Radiocarbon, methane isotopologue and noble gas isotope approaches. *Earth Planet. Sci. Lett.* **585**, 117510 (2022).
27. Beaudry, P., Stefánsson, A., Fiebig, J., Rhim, J. H. & Ono, S. High temperature generation and equilibration of methane in terrestrial geothermal systems: Evidence from clumped isotopologues. *Geochim. Cosmochim. Acta* **309**, 209–234 (2021).
28. Douglas, P. M. J. *et al.* Methane clumped isotopes: Progress and potential for a new isotopic tracer. *Org. Geochem.* **113**, 262–282 (2017).
29. Giovannelli, D. *et al.* Sampling across large-scale geological gradients to study geosphere–biosphere interactions. *Front. Microbiol.* **13**, (2022).
30. Morell, K. D. Late Miocene to recent plate tectonic history of the southern Central America convergent margin. *Geochem. Geophys. Geosystems* **16**, 3362–3382 (2015).
31. Basili, M. *et al.* Subsurface microbial community structure shifts along the geological features of the Central American Volcanic Arc. *PLOS ONE* **19**, e0308756 (2024).
32. Rogers, T. J. *et al.* Chemolithoautotroph distributions across the subsurface of a convergent margin. *ISME J.* 1–11 (2022) doi:10.1038/s41396-022-01331-7.
33. Fullerton, K. M. *et al.* Effect of tectonic processes on biosphere–geosphere feedbacks across a convergent margin. *Nat. Geosci.* **14**, 301–306 (2021).

34. Barry, P. H. *et al.* Forearc carbon sink reduces long-term volatile recycling into the mantle. *Nature* **568**, 487–492 (2019).

35. Barry, P. H. *et al.* Helium, inorganic and organic carbon isotopes of fluids and gases across the Costa Rica convergent margin. *Sci. Data* **6**, 1–8 (2019).

36. Wang, D. T. *et al.* Nonequilibrium clumped isotope signals in microbial methane. *Science* **348**, 428–431 (2015).

37. Ono, S. *et al.* Measurement of a Doubly Substituted Methane Isotopologue, 13CH3D, by Tunable Infrared Laser Direct Absorption Spectroscopy. *Anal. Chem.* **86**, 6487–6494 (2014).

38. Barry, P. H. *et al.* The Helium and Carbon Isotope Characteristics of the Andean Convergent Margin. *Front. Earth Sci.* **10**, (2022).

39. Giovannelli, D., d'Errico, G., Manini, E., Yakimov, M. M. & Vetriani, C. Diversity and phylogenetic analyses of bacteria from a shallow-water hydrothermal vent in Milos island (Greece). *Front. Extreme Microbiol.* **4**, 184 (2013).

40. Callahan, B. J. *et al.* DADA2: High-resolution sample inference from Illumina amplicon data. *Nat. Methods* **13**, 581–583 (2016).

41. Quast, C. *et al.* The SILVA ribosomal RNA gene database project: improved data processing and web-based tools. *Nucleic Acids Res.* **41**, D590–D596 (2012).

42. McMurdie, P. J. & Holmes, S. phyloseq: An R Package for Reproducible Interactive Analysis and Graphics of Microbiome Census Data. *PLOS ONE* **8**, e61217 (2013).

43. Sheik, C. S. *et al.* Identification and Removal of Contaminant Sequences From Ribosomal Gene Databases: Lessons From the Census of Deep Life. *Front. Microbiol.* **9**, (2018).

44. Bolger, A. M., Lohse, M. & Usadel, B. Trimmomatic: a flexible trimmer for Illumina sequence data. *Bioinformatics* **30**, 2114–2120 (2014).

45. Zhu, C. *et al.* Functional sequencing read annotation for high precision microbiome analysis. *Nucleic Acids Res.* **46**, e23–e23 (2018).

46. Menzel, P., Ng, K. L. & Krogh, A. Fast and sensitive taxonomic classification for metagenomics with Kaiju. *Nat. Commun.* **7**, 1–9 (2016).

47. Shuai, Y., Xie, H., Zhang, S., Zhang, Y. & Eiler, J. M. Recognizing the pathways of microbial

methanogenesis through methane isotopologues in the subsurface biosphere. *Earth Planet. Sci. Lett.* **566**, 116960 (2021).

48. Beaudry, P., Stefánsson, A., Fiebig, J., Rhim, J. H. & Ono, S. High temperature generation and equilibration of methane in terrestrial geothermal systems: Evidence from clumped isotopologues. *Geochim. Cosmochim. Acta* **309**, 209–234 (2021).
49. Stolper, D. A. *et al.* Distinguishing and understanding thermogenic and biogenic sources of methane using multiply substituted isotopologues. *Geochim. Cosmochim. Acta* **161**, 219–247 (2015).
50. Yoshinaga, M. Y. *et al.* Carbon isotope equilibration during sulphate-limited anaerobic oxidation of methane. *Nat. Geosci.* **7**, 190–194 (2014).
51. Wolfe, R. S. My kind of biology. *Annu. Rev. Microbiol.* **45**, 1–36 (1991).
52. Thauer, R. Biodiversity and unity in biochemistry. *Antonie Van Leeuwenhoek* **71**, 21–32 (1997).
53. Bertram, P. A. & Thauer, R. K. Thermodynamics of the formylmethanofuran dehydrogenase reaction in Methanobacterium thermoautotrophicum. *Eur. J. Biochem.* **226**, 811–818 (1994).
54. Holmes, A. J., Costello, A., Lidstrom, M. E. & Murrell, J. C. Evidence that participate methane monooxygenase and ammonia monooxygenase may be evolutionarily related. *FEMS Microbiol. Lett.* **132**, 203–208 (1995).
55. Heux, S., Brautaset, T., Vorholt, J. A., Wendisch, V. F. & Portais, J. C. Synthetic Methylotrophy: Past, Present, and Future. in *Methane Biocatalysis: Paving the Way to Sustainability* (eds. Kalyuzhnaya, M. G. & Xing, X.-H.) 133–151 (Springer International Publishing, Cham, 2018). doi:10.1007/978-3-319-74866-5_9.
56. Chiodini, G. *et al.* Geochemistry of the submarine gaseous emissions of Panarea (Aeolian Islands, Southern Italy): magmatic vs. hydrothermal origin and implications for volcanic surveillance. *Pure Appl. Geophys.* **163**, 759–780 (2006).
57. Magnabosco, C. *et al.* The biomass and biodiversity of the continental subsurface. *Nat. Geosci.* 1 (2018) doi:10.1038/s41561-018-0221-6.
58. Cascone, M. *et al.* Microbial diversity in the backarc hot springs of Argentina and its role in biogeochemical cycles. in (GOLDSCHMIDT, 2021).

59. Brazelton, W. J. *et al.* Metagenomic identification of active methanogens and methanotrophs in serpentinite springs of the Voltri Massif, Italy. *PeerJ* **5**, e2945 (2017).

60. Fones, E. M. *et al.* Physiological adaptations to serpentinization in the Samail Ophiolite, Oman. *ISME J.* **13**, 1750–1762 (2019).

61. Ono, S. *et al.* Clumped isotopologue fractionation by microbial cultures performing the anaerobic oxidation of methane. *Geochim. Cosmochim. Acta* **293**, 70–85 (2021).

62. Whiticar, M. J. Carbon and hydrogen isotope systematics of bacterial formation and oxidation of methane. *Chem. Geol.* **161**, 291–314 (1999).

Figures

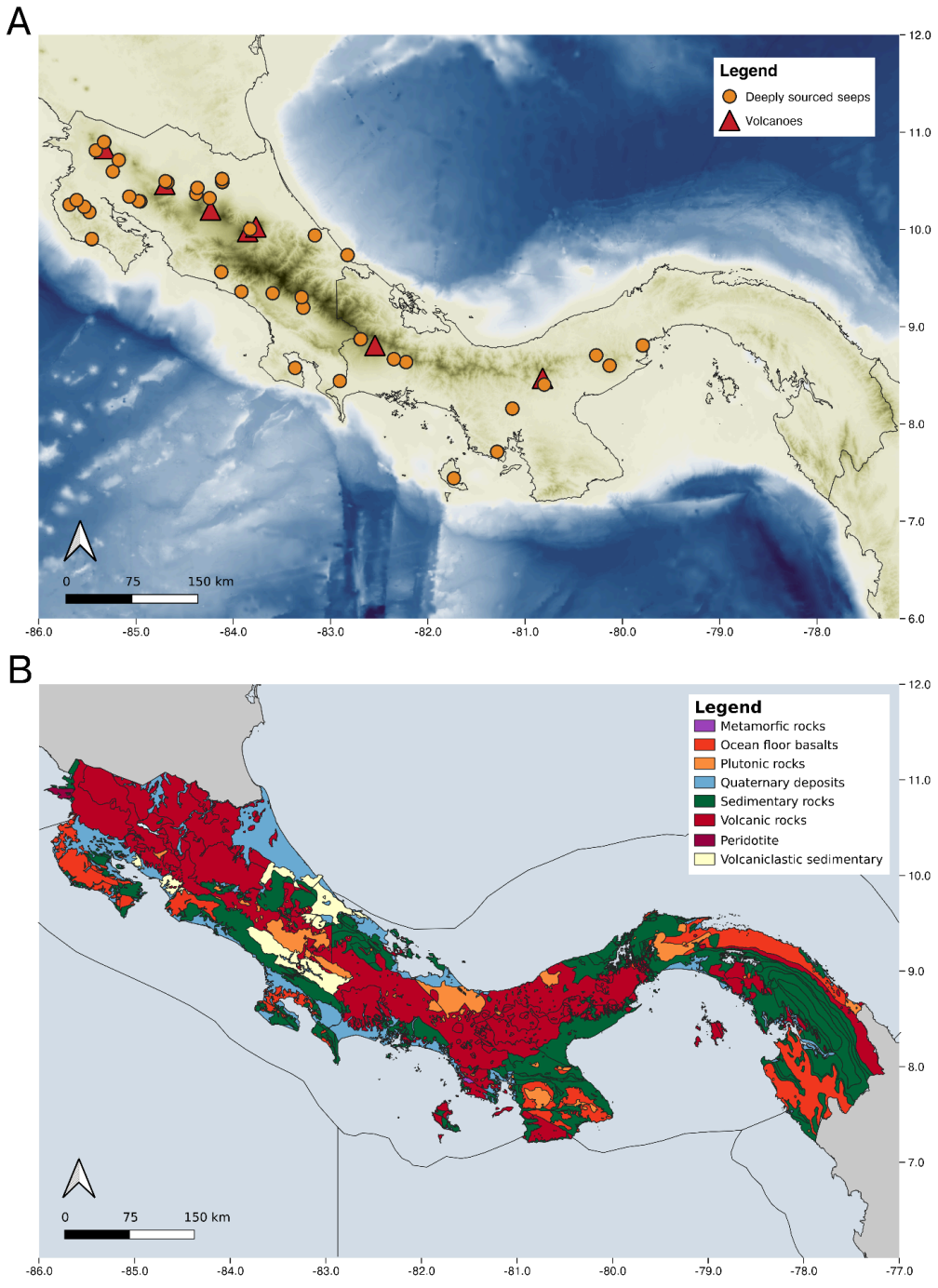

Figure 1. Central America convergent margin maps. A. Topographic map where the sampled sites are indicated as orange circles while volcanoes are indicated as red triangles, from North to South: Rincón de la Vieja, Arenal, Poás, Turrialba, Irazú, Barú, and La Yeguada, respectively. B. Geologic map that includes deposits and different rock types along Costa Rica and Panama.

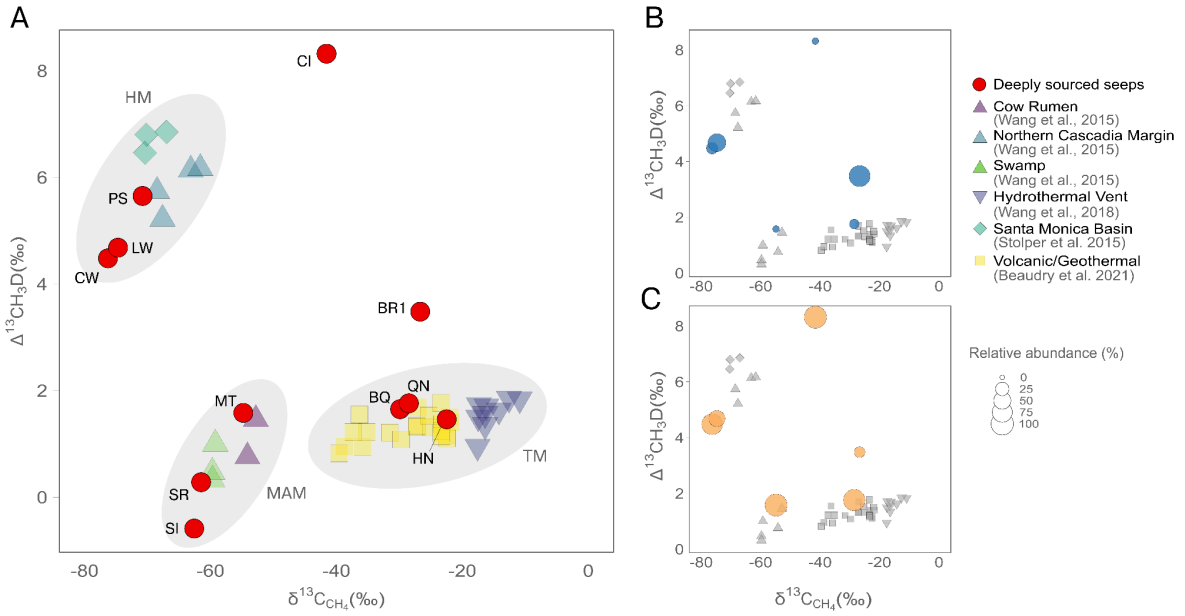

Figure 2. A. Clumped isotopes $\Delta^{13}CH_3D$ values vs $\delta^{13}C_{CH4}$ are shown for 11 deeply sourced springs investigated in Central America (red circles) and compared to samples from different environments (purple triangle: Cow rumen; light blue triangle: Northern Cascadia Margin; green triangle: Swamp; inverted purple triangle: Hydrothermal vents; teal diamond: Santa Monica Basin; yellow square: Volcanic and geothermal samples); B. Relative abundance of aerobic methane cycling related groups (blue) and, C. relative abundance of anaerobic methane cycling related groups (orange), both from 16S rRNA libraries of fluid samples. HM indicates the area of hydrogenotrophic methanogenesis, MAM indicates the area of methylotrophic and acetoclastic methanogenesis, and TM indicates the area of thermogenic methane formation, based on the Whiticar plot (Supplementary Figure S2).

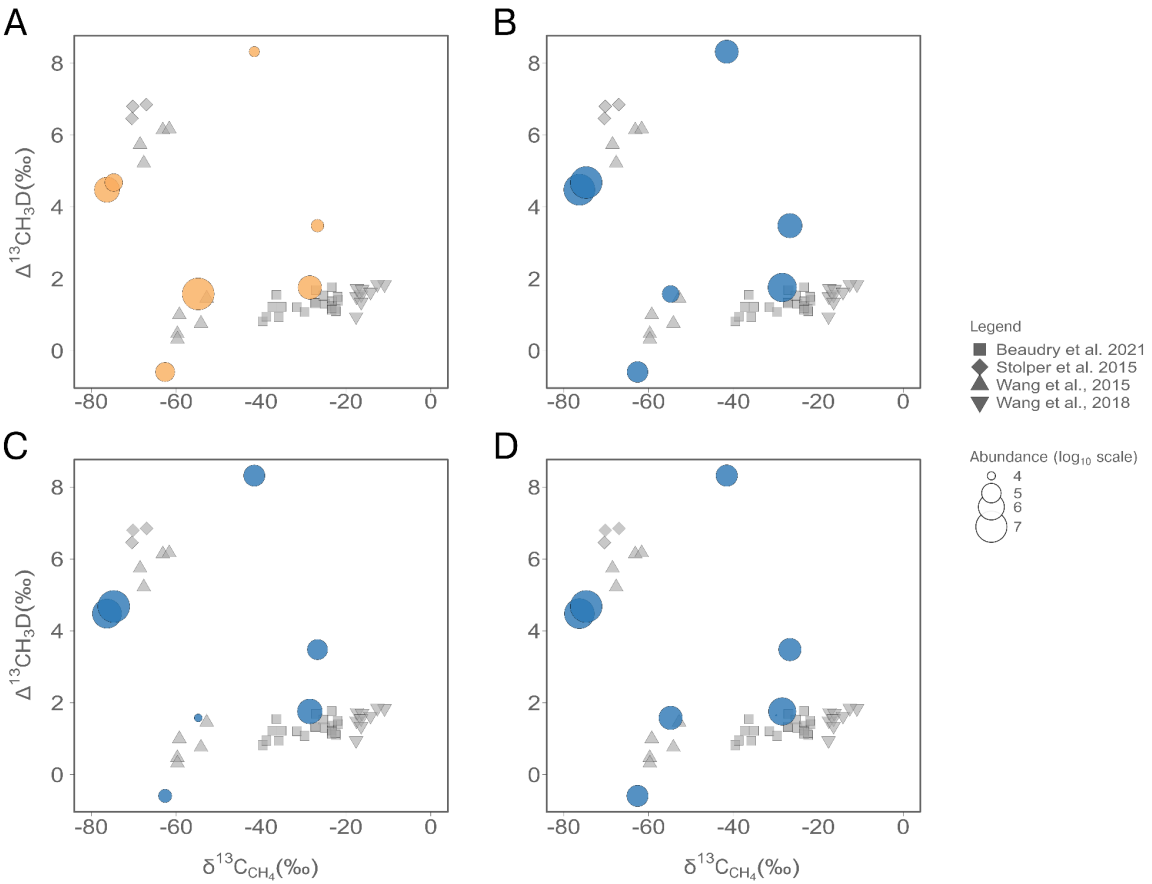

Figure 3. Clumped isotopes $\Delta^{13}CH_3D$ values vs $\delta^{13}C_{CH4}$ are shown for the normalized abundance of the methane cycle key genes found in fluid samples which are reported in orange for the *mcrA* gene (A) and in blue for the *mmo* (B), the *pmo-amo* (C), and the *mdh* (D) genes, the key genes for *bona fide* methane oxidation.

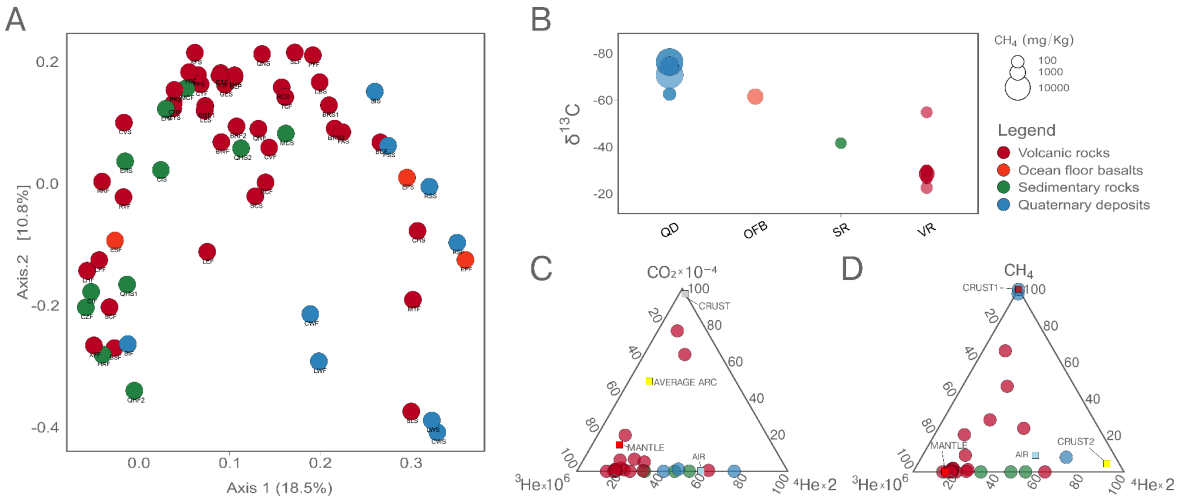

Figure 4. (A) Functional based Principal Coordinates Analysis (PCoA) based on weighted Jaccard similarity of the shotgun metagenome functional read assignment, subsetted for methane cycling; (B) $\delta^{13}C_{CH4}$ distribution across different geologic units (QD: quaternary deposits; OFB: oceanic floor basalts; SR: sedimentary rocks; VR: volcanic rocks) with the size proportional to the CH_4 concentration (mg/kg); (C) Ternary plot of CO_2, ^3He, and ^4He and (D) CH_4, ^3He, and ^4He relative compositions. Mantle, air, and crust gas samples are also reported for comparison. All the figures are colored by geologic units according to the RGB Color Code of the Commission for the Geological Map of the World (CGMW).

Tables

Table 1. Data on the DIC and d13C-DIC, helium isotopes, 4He/20Ne ratio, methane concentrations and methane isotopes for the sampled sites.

Site ID	DIC (mM)	δ^{13}C-DIC (‰)	Rc/Ra	^{4}He/^{20}Ne	CH_4 (mmol/mol)	$\delta^{13}C_{CH}$ (‰)	D_{CH4} (‰)
BC	56.85 ± 4.18	2.34 ± 0.74	3.99	1.51	0.027	na	na
BQ	na ± na	na ± na	5.13	33.24	1.194	-29.9	-175.0
BR1	9.56 ± 0.65	0.23 ± 0.21	6.52	32.29	1.715	-26.7	-234.7
BR2	9.31 ± 0.96	0.96 ± 0.29	na	na	na	na	na
BS	na ± na	na ± na	5.72	4.44	na	na	na
BW	0.36 ± 0.03	-14.14 ± 0.33	na	na	0.379	na	na
CH	37.97 ± 12.15	2.01 ± 0.26	6.39	332.40	0.045	na	na
CI	0.12 ± 0.01	-14.23 ± 0.57	1.31	6.66	0.083	-41.6	-205.3
CL	0.74 ± 0.03	-5.29 ± 0.22	8.86	102.27	2.517	na	na
CV	0.89 ± 0.07	-1.14 ± 0.21	8.37		0.019	na	na
CW	na ± na	na ± na	2.10	22.78	833.635	-76.3	-179.0
CY	5.24 ± 0.79	-4.99 ± 0.50	0.59	1.24	0.002	na	na
CZ	0.86 ± 0.03	-13.62 ± 0.36	na	na	0.031	na	na
EP	0.55 ± 0.06	-21.57 ± 1.78	na	na	3.821	na	na
ER	na ± na	na ± na	6.50	na	0.259	na	na
ES	1.14 ± 0.07	-17.98 ± 0.53	na	na	na	na	na
ET	na ± na	na ± na	na	na	na	na	na
FA	14.22 ± 0.99	2.71 ± 0.26	4.36	14.14	0.019	na	na
GE	1.22 ± 0.05	-18.15 ± 0.40			0.000	na	na
HA	0.12 ± 0.00	-21.19 ± 0.47	1.67	330.52	0.309	na	na
HN	1.12 ± 0.06	-2.84 ± 0.28		87.55	2.580	-22.5	-143.0
LB	17.74 ± 1.39	3.55 ± 0.75	na	na	na	na	na
LE	na ± na	na ± na	na	na	na	na	na
LH	33.54 ± 0.90	-2.20 ± 0.76	7.63	45.58	0.000	na	na
LP	31.33 ± na	-1.47 ± na	7.00	9.11	0.000	na	na
LW	7.11 ± 0.86	-2.95 ± 0.28	1.20	na	157.584	-74.7	-218.2
MC	0.04 ± 0.00	-14.31 ± 0.45	2.36	na	0.630	na	na
MT	21.70 ± 1.10	3.55 ± 0.32	3.57	5.58	0.740	-54.8	-266.9
PF	23.72 ± 4.04	1.24 ± 0.42	1.72	1.30	0.018	na	na
PS	3.18 ± 0.11	-9.32 ± 0.24	3.25	1.32	864.199	-70.8	-205.9
PX	na ± na	na ± na	7.81	5.26	0.003	na	na
QH1	0.11 ± 0.03	-17.98 ± 1.59	3.12	42.36	na	na	na
QH2	0.10 ± 0.05	-9.93 ± 0.83	3.12	27.02	0.047	na	na
QN	2.81 ± 0.16	-1.95 ± 0.38	4.89	1.82	64.677	-28.5	-126.6
RC	1.07 ± 0.03	-5.37 ± 0.23	na	na	4.368	na	na
RR	0.32 ± 0.02	-18.14 ± 0.44	na	na	0.029	na	na
RS	0.25 ± 0.04	-16.04 ± 1.35	2.66	30.67	0.694	na	na
RV	19.73 ± 3.19	-0.28 ± 0.65	6.68	4.38	0.003	na	na
SC	58.45 ± 2.10	3.34 ± 0.26	7.59	4.80	na	na	na
SI	2.24 ± 0.47	-6.43 ± 0.56	0.39	5.05	13.170	-62.6	-327.4
SL	5.69 ± 0.28	-5.28 ± 0.50	3.84	34.70	na	na	na
SR	0.22 ± 0.02	-17.11 ± 1.49	na	na	75.331	-61.5	-352.7
ST	9.94 ± 1.51	-3.88 ± 0.50	na	na	0.004	na	na
TC	13.57 ± 1.10	-2.36 ± 0.74	6.57	76.54	0.941	na	na
VC	6.13 ± 0.30	-1.28 ± 0.17	6.88	50.47	2.022	na	na
XF	na ± na	na ± na	7.62	202.98	na	na	na
YR	0.06 ± 0.00	-21.07 ± 0.46	2.87	na	na	na	na

Supplementary Information

Supplementary Figures

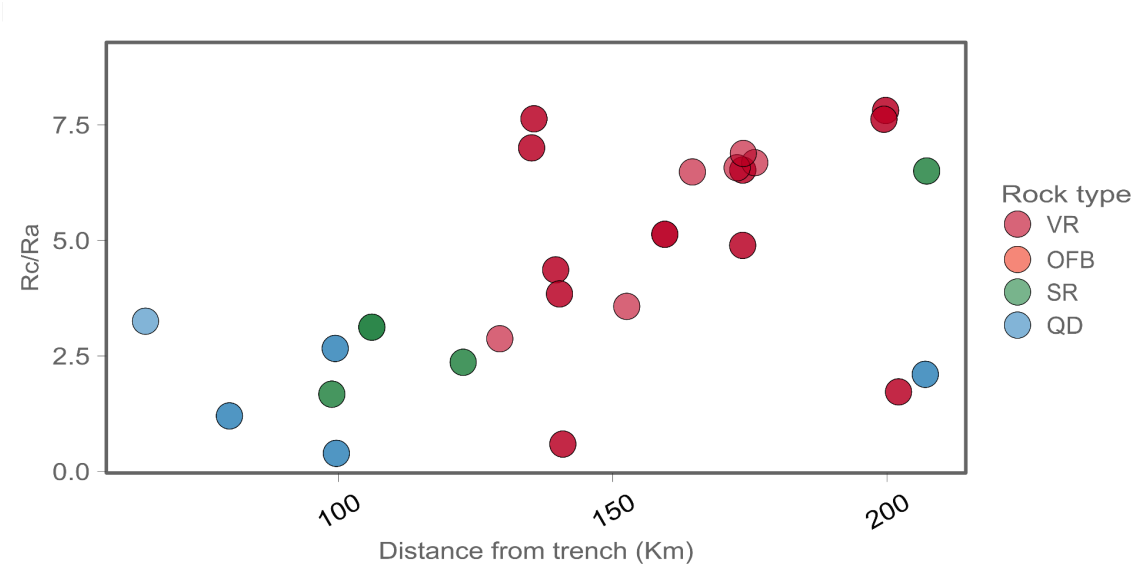

Supplementary figure 1. Rc/Ra plotted against the distance from the trench, coloured by the belonging rock type.

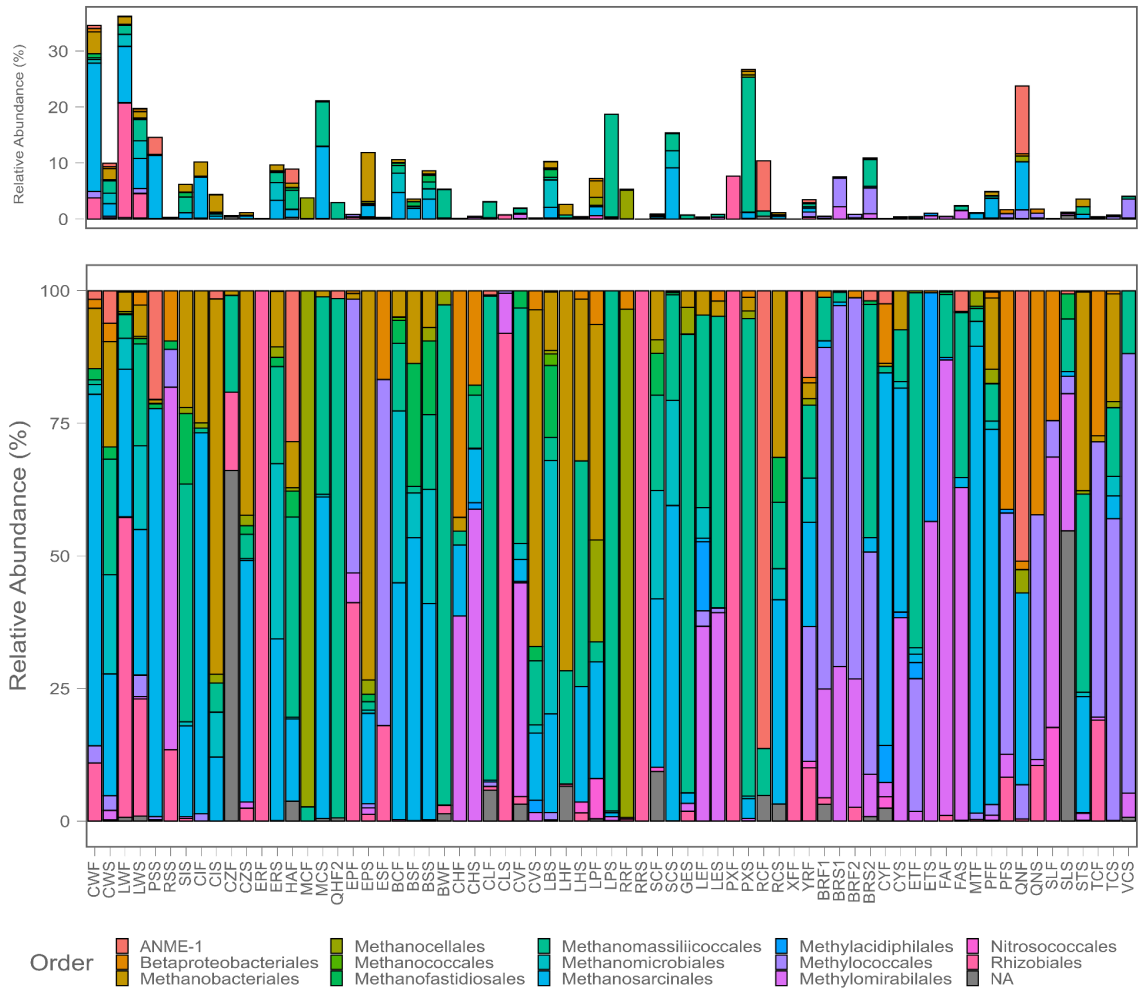

Supplementary Figure S2. Relative abundance of 16S rRNA libraries of methane cycling related taxa at the order level (panel above shows the total relative abundance before the subsetting).

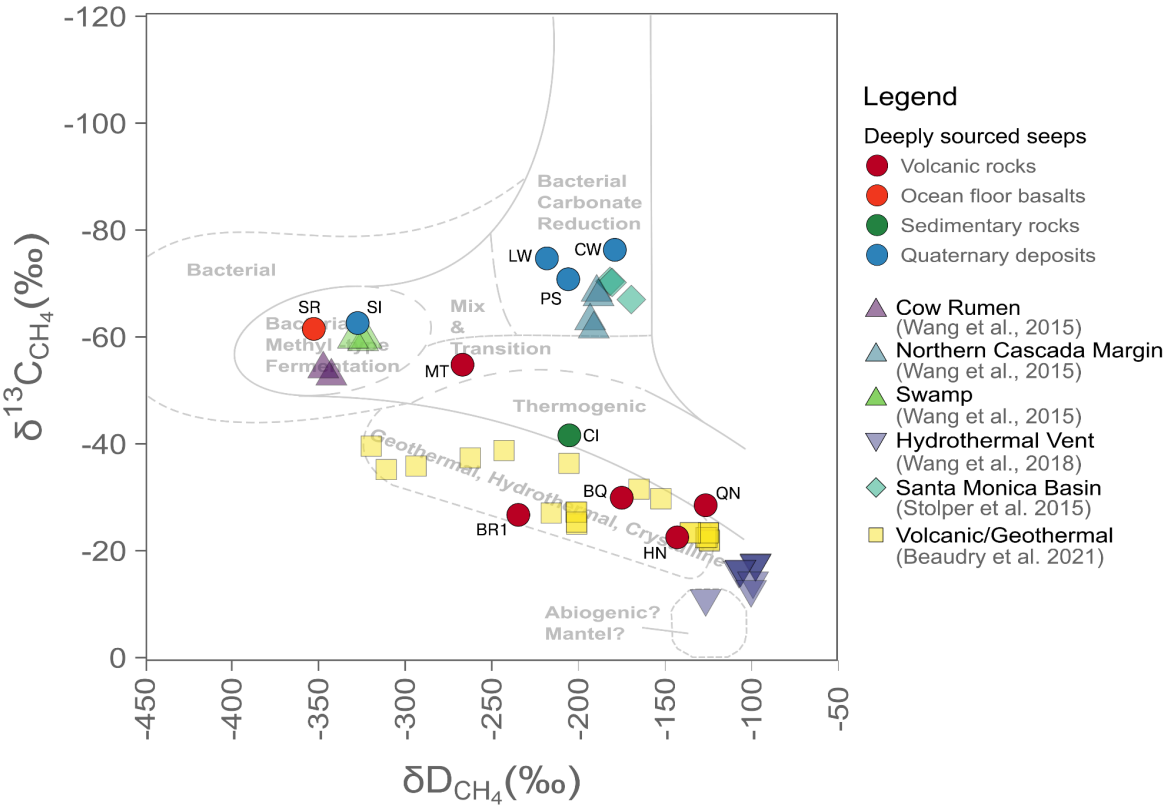

Supplementary Figure S3. Whiticar plot for the Identification of the origin of methane based on the relationship between δD_{CH4} and $\delta^{13}C_{CH4}$ which allow the separation between biogenic and thermogenic gasses from one another. The boundaries that define the common composition space are given from Whiticar, 1999 [62]. From this work, 11 deeply sourced springs, coloured by the belonging geologic unit, are compared to samples from different environments (purple triangle: Cow rumen; light blue triangle: Northern Cascadia Margin; green triangle: Swamp; inverted purple triangle: Hydrothermal vents; teal diamond: Santa Monica Basin; yellow square: Volcanic and geothermal samples).

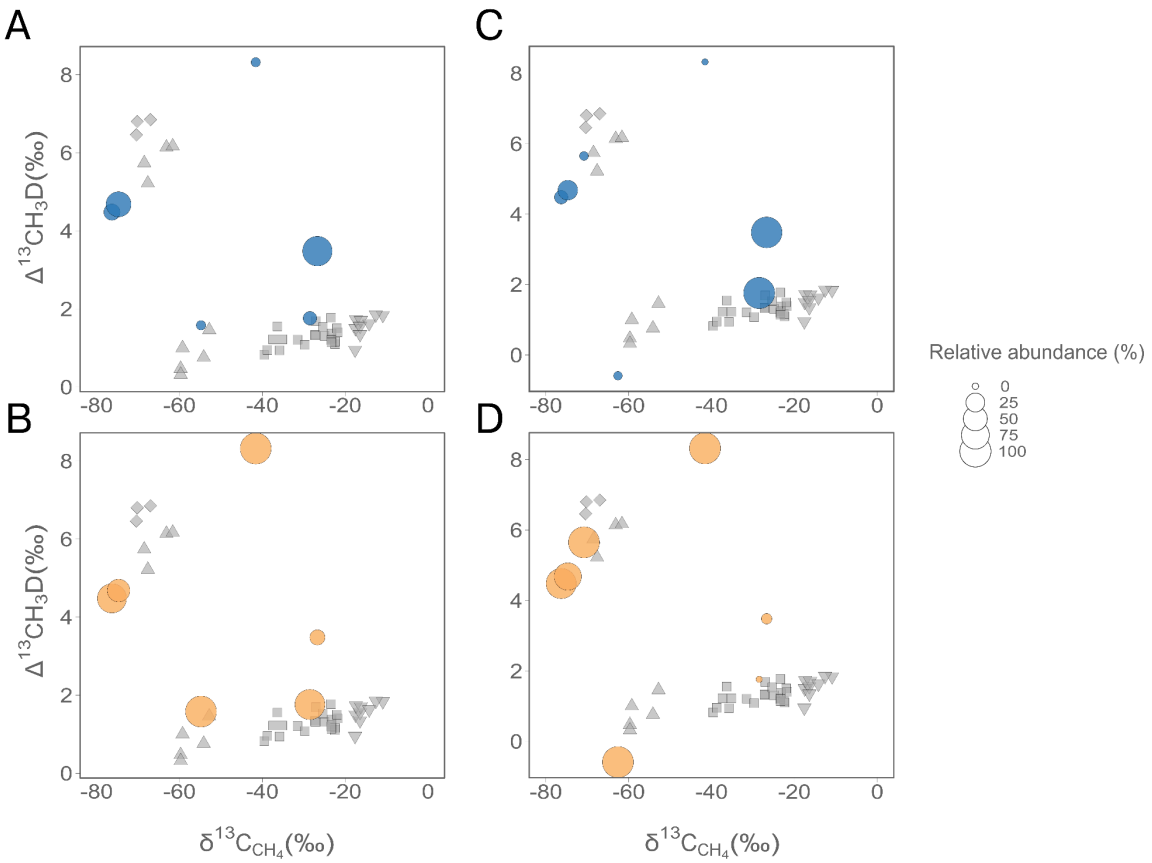

Supplementary Figure S4. Clumped isotopes $\Delta^{13}CH_3D$ values vs $\delta^{13}C_{CH4}$ are shown for fluid (A, B) and sediment (C, D) samples where aerobic (blue) and anaerobic (orange) groups, involved in methane cycling, are present. The relative abundance is obtained from the 16S rRNA libraries of the respective samples and is proportional to the size of the circles.

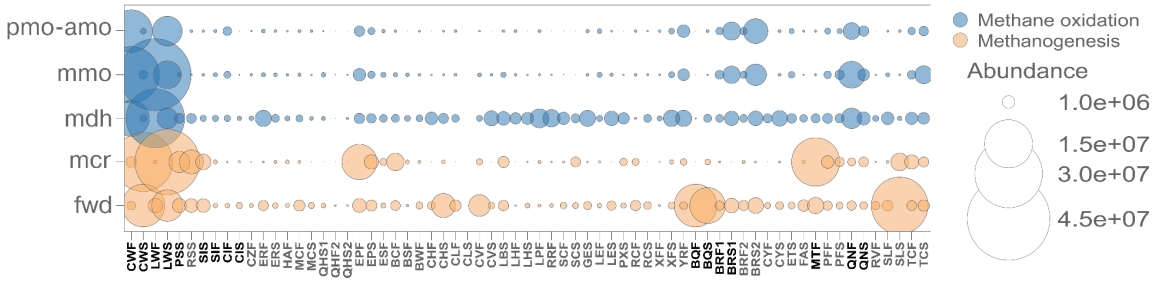

Supplementary Figure S5. Shotgun metagenome functional read assignment for methanogenesis (orange) and methane oxidation (blue). The normalized abundance is indicated as the size of the circles. Sites in which a biogenic signature for the methane was found are highlighted in black.

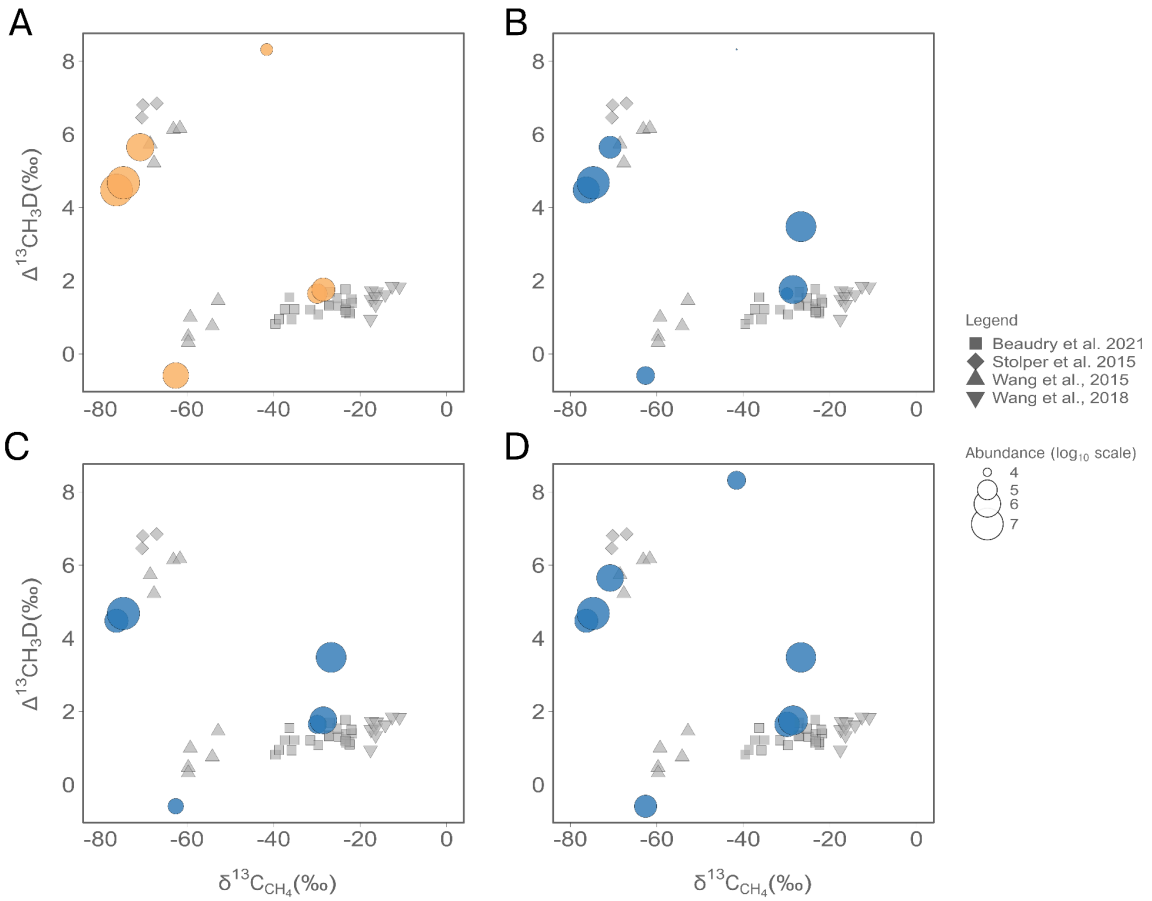

Supplementary Figure S6. Clumped isotopes $\Delta^{13}CH_3D$ values vs $\delta^{13}C_{CH4}$ are shown for the normalized abundance of the methane cycle key genes found in sediment samples. The *mcrA* gene is reported in orange (A), while the *mmo* (B), the *pmo-amo* (C), and the *mdh* (D) genes are reported in blue.

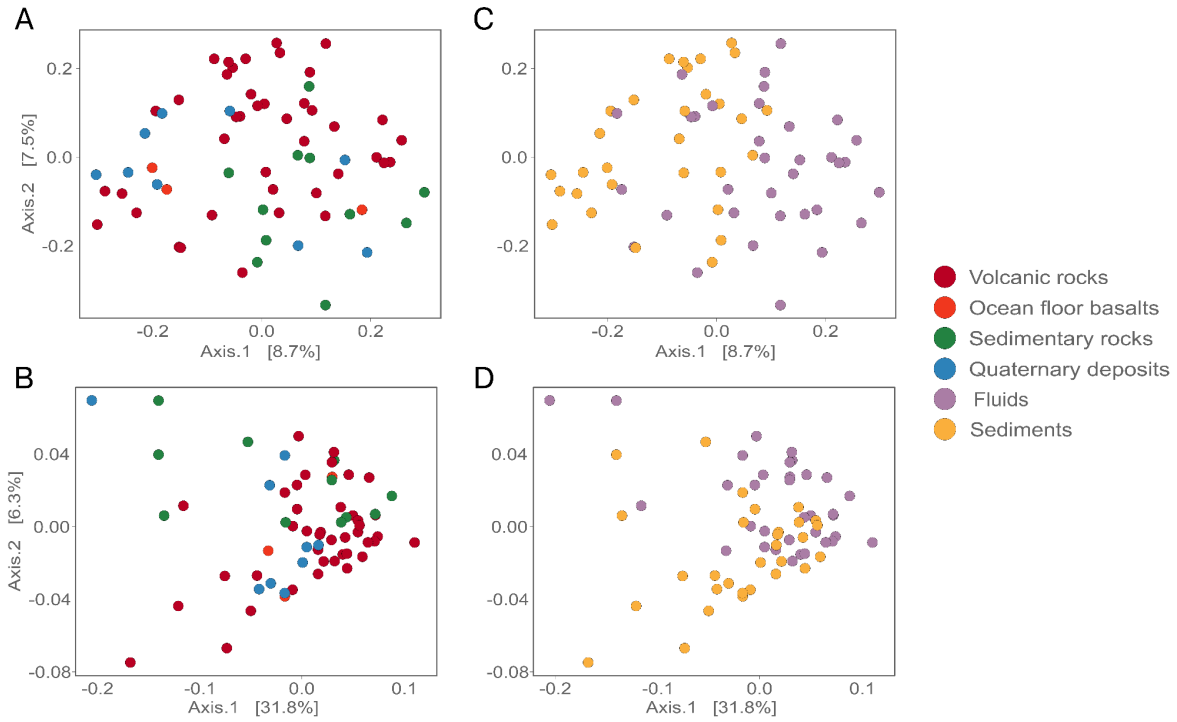

Supplementary Figure S7. Functional based Principal Coordinate Analysis (PCoA) based on (A, C) weighted Jaccard similarity and (B, D) unweighted Jaccard similarity among the shotgun metagenome functional read assignment, coloured by geologic units, and (C, D) by sample type.

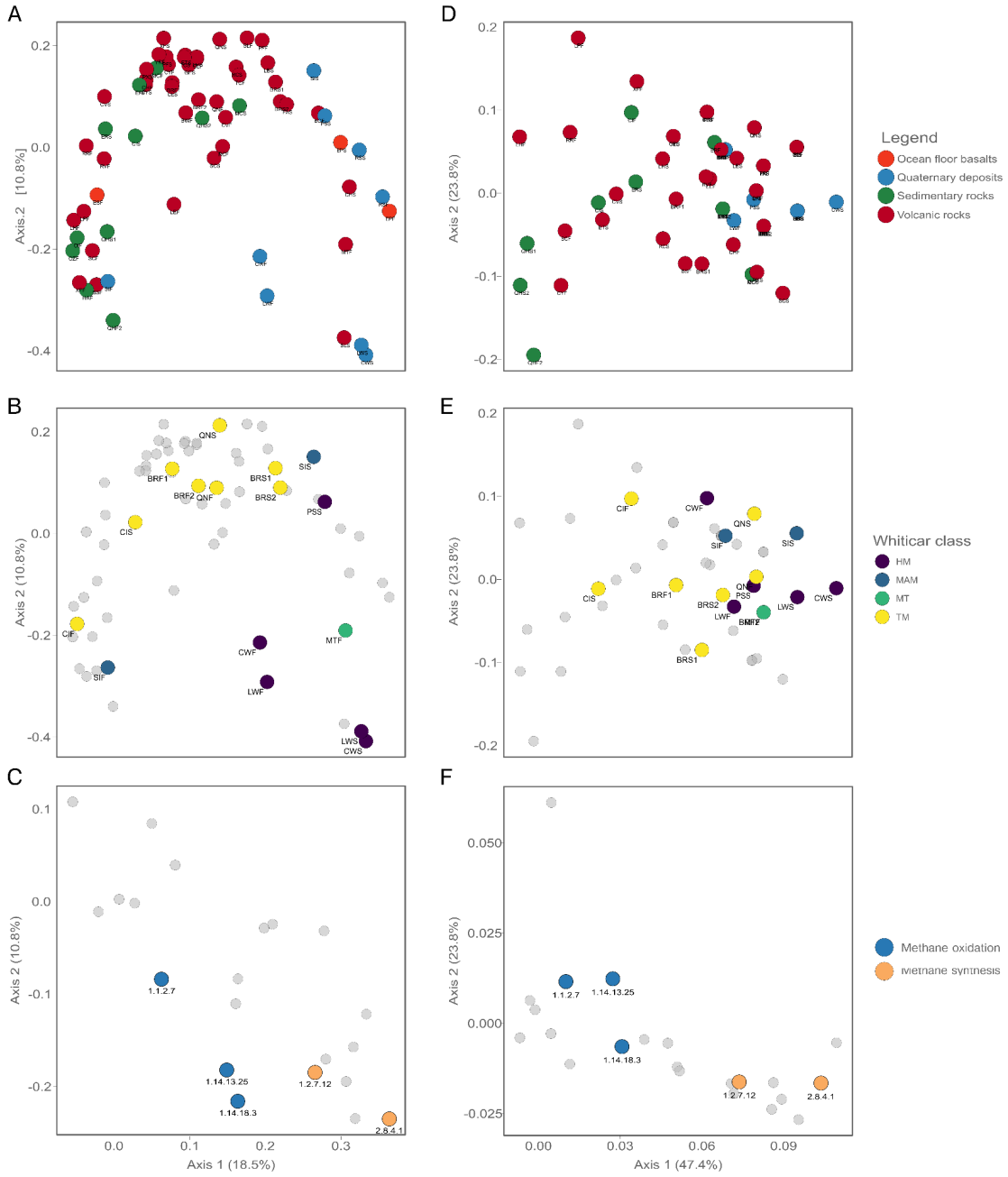

Supplementary Figure S8. PCoA based on weighted Jaccard similarity index on the shotgun metagenome functional read assignment subsetted for methane cycling, coloured by geologic units (A) and whiticar class (B). PCoA based on weighted (C) Jaccard similarity index on the shotgun metagenome functional read assignment subsetted for methane cycling, with main functions for methane synthesis in orange, and main functions for methane oxidation in blue. PCoA based on unweighted (E) Jaccard similarity index on the shotgun metagenome functional read assignment subsetted for methane cycling, coloured by Whiticar class (Supplementary figure 3). PCoA based on unweighted Jaccard similarity index on the shotgun metagenome functional read assignment subsetted for methane cycling, coloured by geologic units (D) and whiticar class (E). PCoA based on unweighted (F) Jaccard similarity index on the shotgun metagenome functional read assignment subsetted for methane cycling, with main functions for methane synthesis in orange, and main functions for methane oxidation in blue.

Supplementary tables

Table 1. Sampled sites location, temperature, pH and salinity.

SiteID	Province	Nation	Geologic unit	Lat	Long	Alt	Temp (°C)	pH	Salinity
BQ	Active volcanic arc	Costa_Rica	Volcanic rocks	10.81	-85.41	535	88.9	2.11	5.73
BR1	Active volcanic arc	Costa_Rica	Volcanic rocks	10.90	-85.33	437	59.0	6.16	3.25
BR2	Active volcanic arc	Costa_Rica	Volcanic rocks	10.90	-85.33	434	53.8	5.87	3.25
CY	Active volcanic arc	Costa_Rica	Volcanic rocks	10.29	-84.96	184	72.0	6.31	6.79
EP	Costa Rica outer forearc	Costa_Rica	Ocean floor basalts	9.90	-85.45	126	26.4	9.99	0.17
ES	Costa Rica outer forearc	Costa_Rica	Ocean floor basalts	9.90	-85.45	122	27.9	9.75	0.20
ET	Active volcanic arc	Costa_Rica	Volcanic rocks	10.48	-84.68	368	40.0	6.06	0.97
FA	Active volcanic arc	Costa_Rica	Volcanic rocks	10.34	-85.07	109	55.2	5.93	6.39
MT	Active volcanic arc	Costa_Rica	Volcanic rocks	10.60	-85.24	166	59.1	6.32	7.21
PF	Active volcanic backarc	Costa_Rica	Volcanic rocks	10.52	-84.12	53	28.7	5.81	4.18
QH1	Costa Rica outer forearc	Costa_Rica	Sedimentary rocks	9.56	-84.12	298	48.7	8.53	NA
QH2	Costa Rica outer forearc	Costa_Rica	Sedimentary rocks	9.56	-84.12	300	36.7	8.69	1.39
QN	Active volcanic arc	Costa_Rica	Volcanic rocks	10.50	-84.70	429	22.9	5.60	0.17
RS	Costa Rica outer forearc	Costa_Rica	Quaternary deposits	10.23	-85.53	82	29.4	9.96	0.13
RV	Active volcanic arc	Costa_Rica	Volcanic rocks	10.32	-84.24	557	42.7	6.19	62.86
SI	Costa Rica outer forearc	Costa_Rica	Quaternary deposits	10.30	-85.61	36	35.9	9.83	1.82
SL	Active volcanic arc	Costa_Rica	Volcanic rocks	10.29	-84.97	165	57.0	6.12	1.46
ST	Active volcanic arc	Costa_Rica	Volcanic rocks	10.00	-83.83	2209	55.8	4.51	2.98
TC	Active volcanic arc	Costa_Rica	Volcanic rocks	10.37	-84.38	553	60.0	6.24	1.84
VC	Active volcanic arc	Costa_Rica	Volcanic rocks	10.90	-85.33	436	59.8	5.00	7.19
BC	Active volcanic arc	Panama	Volcanic rocks	8.81	-79.79	18	31.8	7.50	23.87
BS	Cordillera Talamanca	Panama	Volcanic rocks	8.67	-82.35	360	40.9	9.05	3.10
BW	Cordillera Talamanca	Panama	Volcanic rocks	8.67	-82.35	NA	43.2	NA	3.13
CH	Panama slab window	Panama	Volcanic rocks	8.71	-80.27	216	31.1	7.00	15.30
CI	Panama slab window	Panama	Sedimentary rocks	7.44	-81.73	50	48.3	9.00	1.11
CL	Panama slab window	Panama	Volcanic rocks	8.40	-80.80	289	50.9	7.50	3.26
CV	Panama slab window	Panama	Volcanic rocks	8.60	-80.13	639	34.9	7.46	3.75
CW	Active volcanic backarc	Costa_Rica	Quaternary deposits	9.74	-82.83	8	35.0	7.19	NA
CZ	Panama slab window	Panama	Sedimentary rocks	7.71	-81.29	60	26.3	10	0.22
ER	Active volcanic backarc	Costa_Rica	Sedimentary rocks	9.94	-83.16	89	35.0	3.50	NA
GE	Cordillera Talamanca	Costa_Rica	Volcanic rocks	9.19	-83.28	456	35.8	7.80	0.45
HA	Cordillera Talamanca	Costa_Rica	Sedimentary rocks	9.36	-83.92	118	33.0	8.90	4.97
LB	Panama slab window	Panama	Volcanic rocks	8.81	-79.79	26	34.8	NA	25.35
LE	Cordillera Talamanca	Costa_Rica	Volcanic rocks	10.43	-84.37	153	34.7	6.50	NA
LH	Cordillera Talamanca	Panama	Volcanic rocks	8.87	-82.69	1676	55.4	6.70	8.43
LP	Cordillera Talamanca	Panama	Volcanic rocks	8.87	-82.69	1651	39.1	6.50	5.88
LW	Costa Rica outer forearc	Costa_Rica	Quaternary deposits	8.44	-82.90	32	31.5	7.10	0.55
MC	Cordillera Talamanca	Costa_Rica	Sedimentary rocks	9.34	-83.60	812	31.8	9.60	2.33
PS	Active volcanic backarc	Costa_Rica	Quaternary deposits	8.58	-83.36	2	33.0	8.20	69.20
PX	Active volcanic backarc	Costa_Rica	Volcanic rocks	10.49	-84.11	68	28.7	6.00	NA
RC	Cordillera Talamanca	Costa_Rica	Volcanic rocks	9.30	-83.30	943	60.0	7.70	2.83
RR	Cordillera Talamanca	Panama	Volcanic rocks	8.64	-82.22	792	41.3	NA	2.51
SC	Panama slab window	Panama	Volcanic rocks	8.16	-81.13	136	29.9	6.50	56.21
XF	Active volcanic backarc	Costa_Rica	Volcanic rocks	10.49	-84.11	74	28.9	7.00	NA
HN	Active volcanic backarc	Costa_Rica	Volcanic rocks	10.71	-85.18	765	87.9	1.82	7.09
SR	Costa Rica outer forearc	Costa_Rica	Ocean floor basalts	10.25	-85.68	66	33.0	9.06	NA
YR	Cordillera Talamanca	Costa_Rica	Volcanic rocks	9.19	-83.28	469	26.0	8.90	4.59

Table 2. Methane concentrations and isotopic values of carbon and hydrogen the methane. Calculated equilibrium temperatures from clumped isotope data is also included.

SiteID	CH_4 (ppm)	$\delta^{13}C_{CH4}$	δD_{CH4}	$\Delta^{13}CH_3D$	Calc. Temp Clumped (°C)
BR1	1.7	-26.7	-234.7	3.48	122
QN	64.7	-28.5	-126.6	1.76	280
BQ	1.2	-29.9	-175	1.65	296
MT	0.7	-54.8	-266.9	1.58	307
HN	2.6	-22.5	-143	1.46	328
SR	75.3	-61.5	-352.7	0.28	817
SI	13.2	-62.6	-327.4	-0.59	NA
CI	0.1	-41.6	-205.3	8.05	-37
PS	864.2	-70.8	-205.9	5.65	27
LW	157.6	-74.7	-218.2	4.68	63
CW	833.6	-76.3	-179	4.48	71